The SAURON project – IV. The mass-to-light ratio, the virial mass estimator and the Fundamental Plane of elliptical and lenticular galaxies

Michele Cappellari,[1]* R. Bacon,[2] M. Bureau,[3] M. C. Damen,[1] Roger L. Davies,[3] P. T. de Zeeuw,[1] Eric Emsellem,[2] Jesús Falcón-Barroso,[1] Davor Krajnović,[3] Harald Kuntschner,[4] Richard M. McDermid,[1] Reynier F. Peletier,[5] Marc Sarzi,[3] Remco C. E. van den Bosch[1] and Glenn van de Ven[1]

[1]*Leiden Observatory, Postbus 9513, 2300 RA Leiden, the Netherlands*
[2]*Centre de Recherche Astrophysique de Lyon, 9 Avenue Charles André, 69230 Saint Genis Laval, France*
[3]*Denys Wilkinson Building, University of Oxford, Keble Road, Oxford OX1 3RH*
[4]*Space Telescope European Coordinating Facility, European Southern Observatory, Karl-Schwarzschild-Str 2, 85748 Garching, Germany*
[5]*Kapteyn Astronomical Institute, Postbus 800, 9700 AV Groningen, the Netherlands*

ABSTRACT

We investigate the well-known correlations between the dynamical mass-to-light ratio (M/L) and other global observables of elliptical (E) and lenticular (S0) galaxies. We construct two-integral Jeans and three-integral Schwarzschild dynamical models for a sample of 25 E/S0 galaxies with SAURON integral-field stellar kinematics to about one effective (half-light) radius R_e. They have well-calibrated I-band *Hubble Space Telescope* WFPC2 and large-field ground-based photometry, accurate surface brightness fluctuation distances, and their observed kinematics is consistent with an axisymmetric intrinsic shape. All these factors result in an unprecedented accuracy in the M/L measurements. We find a tight correlation of the form $(M/L) = (3.80 \pm 0.14) \times (\sigma_e/200 \, \text{km s}^{-1})^{0.84 \pm 0.07}$ between the M/L (in the I band) measured from the dynamical models and the luminosity-weighted second moment σ_e of the LOSVD within R_e. The observed rms scatter in M/L for our sample is 18 per cent, while the inferred intrinsic scatter is ∼13 per cent. The (M/L)–σ_e relation can be included in the remarkable series of tight correlations between σ_e and other galaxy global observables. The comparison of the observed correlations with the predictions of the Fundamental Plane (FP), and with simple virial estimates, shows that the 'tilt' of the FP of early-type galaxies, describing the deviation of the FP from the virial relation, is almost exclusively due to a real M/L variation, while structural and orbital non-homology have a negligible effect. When the photometric parameters are determined in the 'classic' way, using growth curves, and the σ_e is measured in a large aperture, the virial mass appears to be a reliable estimator of the mass in the central regions of galaxies, and can be safely used where more 'expensive' models are not feasible (e.g. in high-redshift studies). In this case the best-fitting virial relation has the form $(M/L)_{\text{vir}} = (5.0 \pm 0.1) \times R_e \sigma_e^2/(LG)$, in reasonable agreement with simple theoretical predictions. We find no difference between the M/L of the galaxies in clusters and in the field. The comparison of the dynamical M/L with the $(M/L)_{\text{pop}}$ inferred from the analysis of the stellar population, indicates a median dark matter fraction in early-type galaxies of ∼30 per cent of the total mass inside one R_e, in broad agreement with previous studies, and it also shows that the stellar initial mass function varies little among different galaxies. Our results suggest a variation in M/L at constant $(M/L)_{\text{pop}}$, which seems to be linked to the galaxy dynamics. We speculate that fast-rotating galaxies have lower dark matter fractions than the slow-rotating and generally more-massive ones. If correct, this would suggest a connection between the galaxy

*E-mail: cappellari@strw.leidenuniv.nl

assembly history and the dark matter halo structure. The tightness of our correlation provides some evidence against cuspy nuclear dark matter profiles in galaxies.

Key words: galaxies: elliptical and lenticular, cD – galaxies: evolution – galaxies: formation – galaxies: kinematics and dynamics – galaxies: structure.

1 INTRODUCTION

Early-type galaxies display a large variety of morphologies and kinematics. Some of them show little rotation, significant kinematic twists, and kinematically decoupled components in their centres. These systems are generally classified as ellipticals (E) from photometry alone, and are more common among the most massive objects, which also tend to be redder, metal-rich and to appear nearly round on the sky. The remaining early-type galaxies show a well-defined rotation pattern, with a rotation axis generally well aligned with the photometric minor axis. These objects are often less massive, tend to be bluer and can appear very flat on the sky. These galaxies are generally classified either as E or as lenticulars (S0) from photometry (Davies et al. 1983; Franx, Illingworth & de Zeeuw 1991; Kormendy & Bender 1996).

Despite the differences between individual objects, when considering early-type galaxies as a class, it appears that they satisfy a number of regular relations between their global parameters. The first to be discovered was the relation $L \propto \sigma^4$ between the luminosity and the velocity dispersion of the stars in elliptical galaxies (Faber & Jackson 1976). These authors also already realized that, under simple assumptions, the observed relation implies a variation of the mass-to-light ratio (M/L) with galaxy luminosity.

It is now clear that the Faber–Jackson relation is the projection of a thin plane, the Fundamental Plane (FP; Djorgovski & Davis 1987; Dressler et al. 1987), which correlates three global observables: the effective radius R_e, the velocity dispersion σ and the surface brightness I_e at the effective radius. The relation is of the form $R_e \propto \sigma^\alpha I_e^\beta$. If galaxies were homologous stellar systems in virial equilibrium, with constant M/L, one would expect a correlation of the form $R_e \propto \sigma^2 I_e^{-1}$. The observed relation has instead the form $R_e \propto \sigma^{1.24} I_e^{-0.82}$ (Jørgensen, Franx & Kjaergaard 1996), with generally good agreement between different estimates and a weak dependence on the photometric band in the visual region (Bernardi et al. 2003; Colless et al. 2001, and references therein).

One way to explain the observed deviation, or 'tilt', of the FP from the virial predictions is to assume a power-law dependence of the M/L on the other galaxy structural parameters (mainly, galaxy mass). The M/L variation could be due to differences in the stellar population or in the dark matter fraction in different galaxies. Other options are also possible however. The virial prediction for the FP is based on the assumption that galaxies form a set of homologous systems, both in the sense of having self-similar density distributions and in terms of having the same orbital distribution. These spatial and dynamical non-homologies could then also explain the observed tilt of the FP. All these possible effects are known to occur in practice, and they must contribute, to some degree, to the observed tilt of the FP (e.g. van Albada, Bertin & Stiavelli 1995).

Various attempts have been made to estimate the contribution of the possible effects, with sometimes contradictory results. A number of authors tried to study the origin of the FP tilt using approximate models. Ciotti, Lanzoni & Renzini (1996) used theoretical arguments to show that non-homology, particularly in the surface-brightness profile of galaxies, could in principle play a major role in the tilt. Subsequent studies concluded that non-homology is indeed significant from the indirect argument that the expected change in M/L of the stellar population alone cannot explain the observed M/L variation (Prugniel & Simien 1996; Forbes, Ponman & Brown 1998; Pahre, Djorgovski & de Carvalho 1998; Forbes & Ponman 1999). From the observed spatial non-homology, namely, the inverse correlation of galaxy concentration and luminosity (Caon, Capaccioli & D'Onofrio 1993; Graham, Trujillo & Caon 2001) various works concluded that the contribution of the spatial non-homology of galaxies of different luminosities is responsible for a significant fraction of the observed FP tilt (Graham & Colless 1997; Prugniel & Simien 1997; Trujillo, Burkert & Bell 2004). These authors constructed simple spherical isotropic models and used large samples of galaxies to estimate the variation in the virial M/L from the variation of the shape of galaxy profiles with luminosity. Although changes in the light-profile shape do not, on their own, significantly affect the tilt of the FP (e.g. Trujillo, Graham & Caon 2001) they produce a variation in the velocity-dispersion profile which may influence the measured M/L.

van der Marel (1991), Magorrian et al. (1998) and Gerhard et al. (2001) constructed detailed dynamical models of smaller samples of galaxies, reproducing in detail the photometry and long-slit spectroscopy observations. They also investigated the M/L and concluded that the variations observed in the models are consistent with the observed FP tilt. However, the fact that the spread in their measured M/L values was much larger than that in the FP, made the results inconclusive.

In this work we revisit what was done in the latter studies, with some crucial differences.

(i) The quality of our data allows a dramatic improvement in the accuracy of the dynamical M/L determinations; for our galaxy sample SAURON (Bacon et al. 2001, hereafter Paper I) integral-field observations of the stellar kinematics are available, together with *Hubble Space Telescope* (*HST*)/WFPC2 and ground-based MDM photometry in the *I* band (which we reproduce in detail with our models including ellipticity variations), and reliable distances based on the surface brightness fluctuation (SBF) determinations by Tonry et al. (2001).

(ii) Our sample was extracted from the SAURON representative sample of de Zeeuw et al. (2002, hereafter Paper II), which spans a wide range in velocity dispersion and luminosity, and includes both bright and low-luminosity E and S0 galaxies.

(iii) In contrast to previous studies the axisymmetric modelling technique we use can also be applied to very flattened galaxies, or objects containing multiple photometric components.

All these allow us to carefully estimate the intrinsic scatter in the correlations between the dynamical M/L and other galaxy observables, and make it possible to set tight constraints on the measured slopes, for stringent comparisons with previous FP results and predictions of galaxy formation theory.

This paper is organized as follows. In Section 2, we present the sample selection and the photometric and kinematical data used. In Section 3, we describe the two-integral and three-integral dynamical models used to measure the M/L. In Section 4, we study the correlation of the M/L with global galaxy parameters. We discuss our results in Section 5 and summarize our conclusions in Section 6.

2 SAMPLE AND DATA

2.1 Selection

The set of galaxies we use for this work was extracted from the SAURON sample of 48 E and S0 galaxies (classification taken from de Vaucouleurs et al. 1991, hereafter RC3), which is representative of nearby bright early-type galaxies ($cz \leqslant 3000 \, \text{km s}^{-1}$; $M_B \leqslant -18$ mag). As described in Paper II, it contains 24 galaxies in each of the E and S0 subclasses, equally divided between 'cluster' and 'field' objects (the former defined as belonging to the Virgo cluster, the Coma I cloud, or the Leo I group, and the latter being galaxies outside these clusters), uniformly covering the plane of ellipticity, ε, versus absolute blue magnitude, M_B.

One of the requirements for the subsample defined in the present paper was the availability of an accurate distance determined using the SBF technique by Tonry et al. (2001). 38 objects in the SAURON sample satisfy this criterion. The second requirement was the availability of *HST* photometry obtained with the WFPC2 in the *I* band ($F814W$). We selected this band because it is minimally affected by intrinsic dust effects and it is expected to trace well the bulk of the luminous mass in galaxies. 35 galaxies satisfy this second criterion. The intersection between the two groups with SBF distances and *I*-band photometry leads to a sample of 29 galaxies. Out of these galaxies we additionally eliminated the objects showing strong evidence of bars within the SAURON field, from either the photometry (see Section 3.1) or the kinematics. Specifically, we excluded the five galaxies NGC 1023, NGC 2768, NGC 3384, NGC 3489 and NGC 4382. We did not attempt to eliminate all possibly barred galaxies from our sample, but at least we excluded the objects for which it makes little sense to deproject the observed surface density under the assumption of axisymmetry and to fit an axisymmetric model, which has to produce a bi-symmetric velocity field aligned with the photometry. We added the special galaxy M32, which is not part of the representative sample, to the remaining sample of 24 galaxies. This last object allows us to sample the low-luminosity end of our correlations, which by construction cannot be accessed with galaxies from the main survey. This leads to a final sample of 25 galaxies.

2.2 Photometry

Our photometric data consist of the *HST*/WFPC2/$F814W$ images already mentioned, together with ground-based photometry obtained, in the same $F814W$ filter, with the 1.3-m McGraw-Hill Telescope at the MDM observatory on Kitt Peak. A relatively large field of view (FOV) of $17.1 \times 17.1 \, \text{arcmin}^2$ was used for the MDM observations to provide good coverage of the outer parts of our galaxies and to allow for an accurate sky-subtraction from the observed frames. The MDM images are part of a complete photometric survey of the SAURON galaxies, and they will be described in detail elsewhere.

We adopted the WFPC2 images as reference for the photometric calibration and rescaled the MDM images to the same level. For this we measured logarithmically sampled photometric profiles on
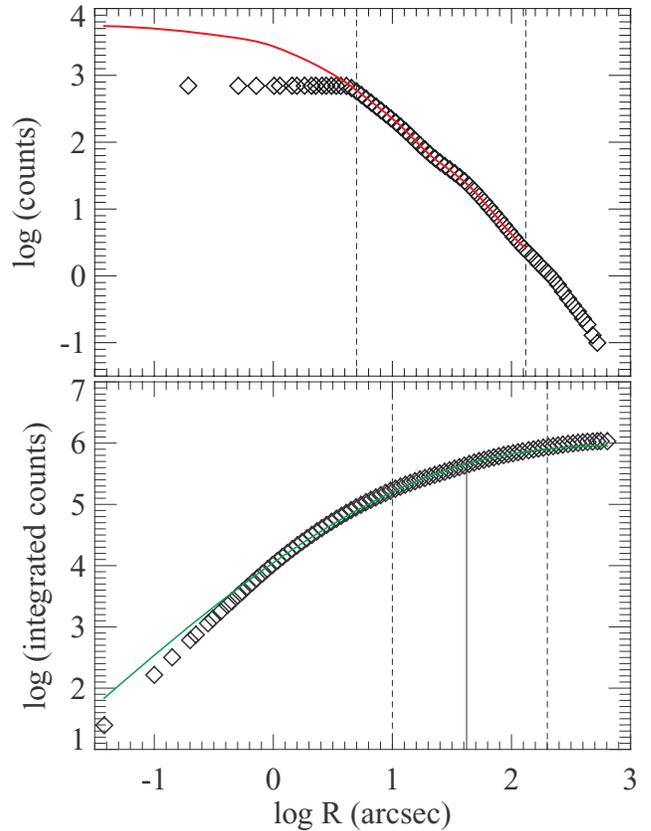
Figure 1. Top panel: match between the photometric profile of NGC 3379 derived from the WFPC2/$F814W$ (red solid line) and MDM images (diamonds). The sky-level of the WFPC2 image and the scaling factor of the MDM image are the free parameters of the fit. The flattening in the central ground-based profile is due to saturation of the image inside $R \lesssim 3$ arcsec. The fit was performed in the region between the two vertical dotted lines, where the WFPC2 and MDM profiles overlap, while excluding the innermost 3 arcsec to avoid PSF and saturation effects. Bottom panel: fit of a de Vaucouleurs $R^{1/4}$ growth curve (green solid line) to the combined WFPC2+MDM observed aperture photometry (diamonds). The two vertical dotted lines define the boundaries of the region that was included in the fit, which is limited to 200 arcsec to reduce uncertainties due to the sky-subtraction and contamination from nearby galaxies or foreground stars. The solid vertical line marks the location of R_e.

the two images, using circular apertures, after masking bright stars or galaxies within the field. The sky level of the wide-field ground-based image can be determined easily and accurately by requiring the profile to tend asymptotically to a power law at large radii. This leaves two free parameters: the scaling ratio between the ground-based image and the WFPC2 image, and the sky level of the WFPC2 image. The two parameters were fitted by minimizing the relative error between the two photometric profiles in the region of overlap, while excluding the innermost 3 arcsec to avoid seeing effects (top panel in Fig. 1). After the fit we merged the two sky-subtracted and scaled profiles into a single one, which was used for the determination of the global photometric parameters (bottom panel in Fig. 1).

We measured the half-light radius R_e and total galaxy luminosity as in classic studies on the FP of early-type galaxies (e.g. Burstein et al. 1987; Jørgensen, Franx & Kjaergaard 1995), namely, from a fit of a de Vaucouleurs $R^{1/4}$ growth curve to the aperture photometry. The fit was generally restricted to radii $R \gtrsim 10$ arcsec where

the growth curve is a good description of the observations. We also experimented with alternatives: (i) fitting a Sérsic (1968) $R^{1/n}$ curve to the profile, (ii) fitting a $R^{1/n}$ growth curve to the aperture photometry, and (iii) fitting a $R^{1/n}$ growth curve, with the value of n fixed by a previous fit to the profile. We found that the values of R_e obtained with different methods differ substantially in some cases. This is not too surprising as the determination is based on an extrapolation of the profile. We adopted the $R^{1/4}$ growth curve fit because it allows a direct comparison of our results with previous works on the FP in Section 4.4. Another advantage is that with a growth curve approach the profile does not have to be well described by the assumed parametrization, but one just tries to extrapolate the luminosity to infinite radius, starting from the outermost measured photometric points. This makes the measurement more robust and better reproducible than a profile-fitting approach. The measured values of the global photometric parameters are given in Table 1.

2.3 Kinematics

The kinematic measurements used here were presented in Emsellem et al. (2004, hereafter Paper III), where further details can be found. In brief, the SAURON integral-field spectroscopic observations, obtained at the 4.2-m William Herschel Telescope on La Palma, were reduced and merged with the XSAURON software developed at Centre de Recherche Astronomique de Lyon (CRAL: Paper I. They where spatially binned to a minimum signal-to-noise ratio (S/N) ≈ 60 using the Voronoi two-dimensional binning algorithm by Cappellari & Copin (2003) and the stellar kinematics were subsequently extracted with the penalized pixel-fitting (PPXF) method of Cappellari & Emsellem (2004). This provided, for each Voronoi bin, the mean velocity V, the velocity dispersion σ and four higher-order Gauss–Hermite moments of the velocity from h_3 to h_6 (Gerhard 1993; van der Marel & Franx 1993). We estimated errors on the kinematics using 100 Monte Carlo realizations and applying the

Table 1. Galaxy sample and measured parameters.

Galaxy name	R_e (arcsec)	R_{max}/R_e	I_T (mag)	K_T (mag)	σ'_e (km s^{-1})	i (°)	$(M/L)_{Jeans}$ (I-band)	$(M/L)_{Schw}$ (I-band)	$(M/L)_{pop}$ (I-band)	$(m-M)$ (mag)	A_B (mag)	Fast-rotator?
(1)	(2)	(3)	(4)	(5)	(6)	(7)	(8)	(9)	(10)	(11)	(12)	(13)
NGC 221 (M32)	30	0.92	7.07	5.09	60	50	1.25	1.41	1.17	24.49±0.08	0.35	yes
NGC 524	51	0.61	8.76	7.16	235	19	5.04	4.99	3.00	31.84±0.20	0.36	yes
NGC 821	39	0.62	9.47	7.90	189	90	3.54	3.08	2.60	31.85±0.17	0.47	yes
NGC 2974	24	1.04	9.43	8.00	233	57	4.47	4.52	2.34	31.60±0.24	0.23	yes
NGC 3156	25	0.80	10.97	9.55	65	67	1.70	1.58	0.62	31.69±0.14	0.15	yes
NGC 3377	38	0.53	8.98	7.44	138	90	2.32	2.22	1.75	30.19±0.09	0.15	yes
NGC 3379 (M105)	42	0.67	8.03	6.27	201	90	3.14	3.36	3.08	30.06±0.11	0.10	yes
NGC 3414	33	0.60	9.57	7.98	205	90	4.06	4.26	2.91	31.95±0.33	0.10	no
NGC 3608	41	0.49	9.40	8.10	178	90	3.62	3.71	2.57	31.74±0.14	0.09	no
NGC 4150	15	1.39	10.51	8.99	77	52	1.56	1.30	0.66	30.63±0.24	0.08	yes
NGC 4278	32	0.82	8.83	7.18	231	45	4.54	5.24	3.05	30.97±0.20	0.12	yes
NGC 4374 (M84)	71	0.43	7.69	6.22	278	90	4.16	4.36	3.08	31.26±0.11	0.17	no
NGC 4458	27	0.74	10.68	9.31	85	90	2.33	2.28	2.27	31.12±0.12	0.10	no
NGC 4459	38	0.71	8.91	7.15	168	47	2.76	2.51	1.86	30.98±0.22	0.20	yes
NGC 4473	27	0.92	8.94	7.16	192	73	3.26	2.91	2.88	30.92±0.13	0.12	yes
NGC 4486 (M87)	105	0.29	7.23	5.81	298	90	5.19	6.10	3.33	30.97±0.16	0.10	no
NGC 4526	40	0.66	8.41	6.47	222	79	3.51	3.35	2.62	31.08±0.20	0.10	yes
NGC 4550	14	1.45	10.40	8.69	110	78	2.81	2.62	1.44	30.94±0.20	0.17	yes
NGC 4552 (M89)	32	0.63	8.54	6.73	252	90	4.52	4.74	3.35	30.87±0.14	0.18	no
NGC 4621 (M59)	46	0.56	8.41	6.75	211	90	3.25	3.03	3.12	31.25±0.20	0.14	yes
NGC 4660	11	1.83	9.96	8.21	185	70	3.63	3.63	2.96	30.48±0.19	0.14	yes
NGC 5813	52	0.52	9.12	7.41	230	90	4.19	4.81	2.97	32.48±0.18	0.25	no
NGC 5845	4.6	4.45	11.10	9.11	239	90	3.17	3.72	2.96	32.01±0.21	0.23	yes
NGC 5846	81	0.29	8.41	6.93	238	90	4.84	5.30	3.33	31.92±0.20	0.24	no
NGC 7457	65	0.39	9.45	8.19	78	64	1.86	1.78	1.12	30.55±0.21	0.23	yes

Notes. Column (1): NGC number. Column (2): effective (half-light) radius R_e measured in the I band from *HST*/WFPC2 + MDM images. Comparison with published values shows an rms scatter of 17 per cent. Column (3): ratio between the maximum radius R_{max} sampled by the kinematical observations and R_e. We defined $R_{max} \equiv \sqrt{A/\pi}$, where A is the area on the sky sampled by the SAURON observations. Column (4): total observed I-band galaxy magnitude. Comparison with the corresponding values by Tonry et al. (2001) indicates an observational error of 13 per cent. Column (5): total observed K-band galaxy magnitude, from the 2MASS XSC (Jarrett et al. 2000). Column (6): velocity dispersion derived with PPXF, by fitting a purely Gaussian LOSVD to the luminosity-weighted spectrum within R_e. For the galaxies in which $R_{max}/R_e < 1$ this value was determined on the whole SAURON field. Equation (1) was used to derive the σ_e value used in our correlations, adopting as R/R_e the value in column (3). The statistical errors on these values are negligible, but we adopt an error of 5 per cent to take systematics into account. Column (7): inclination of the best-fitting two-integral Jeans model. We do not attach errors as they are fully model-dependent. Column (8): M/L of the best-fitting two-integral Jeans model. Column (9): M/L of the best-fitting three-integral Schwarzschild model, computed at the inclination of column (7). Comparison with column (8) suggests an error of 6 per cent in these values. Column (10): stellar population $(M/L)_{pop}$ determined from measured line-strength values using SSP models. The median formal error on this quantity is $\sim$10 per cent, but this value is strongly assumption-dependent. See Section 3.3 for details. Column (11): galaxy distance modulus of Tonry et al. (2001), adjusted to the Cepheid zero-point of Freedman et al. (2001) by *subtracting* 0.06 mag [for a discussion see section 3.3 of Mei et al. (2005)]. Column (12): B-band galactic extinction of Schlegel, Finkbeiner & Davis (1998) as given by the NED database. We adopt $A_I = A_B/2.22$ as in NED. (13) Galaxy classification according to the measured value of the specific stellar angular momentum within one R_e, from the SAURON kinematics. A qualitative distinction between the two classes of galaxies can be seen on the kinematic maps of Paper III. More details will be given in Emsellem et al. (in preparation).

prescriptions of section 3.4 of Cappellari & Emsellem (2004). In addition we observed M32 with SAURON in 2003 August with the same configuration as for the other galaxies in Paper III, and obtained two pointings resulting in an FOV of about 40×60 arcsec^2.

For each galaxy in our sample we determined σ_e, the luminosity-weighted second moment of the line-of-sight velocity distribution (LOSVD) within the half-light radius R_e. Compared to the central velocity dispersion σ_c, which was sometimes used before, this quantity has the advantage that it is only weakly dependent on the details of the aperture used. The observed σ_e is an approximation to the second velocity moment which appears in the virial equation (Binney & Tremaine 1987, Section 4.3). It is proportional to $\sqrt{M}$ (with M the galaxy mass), and so is weakly dependent on the details of the orbital distribution. These are the reasons why a similar quantity (estimated, however, from long-slit data) was also adopted by, for example, Gebhardt et al. (2000) to study the correlation between the mass of supermassive black holes (BHs) and the velocity dispersion of the host galaxy.

The use of integral-field observations allows us to perform the σ_e measurements in a more rigorous manner than was possible with long slits. We measured σ_e from the data by co-adding all luminosity-weighted *spectra* within R_e. The resulting single 'effective spectrum' has extremely high S/N $\gtrsim 300$ per spectral element, and is equivalent to what would have been observed with a single aperture of radius R_e centred on the galaxy. We then used PPXF, with the same set of multiple templates from Vazdekis (1999, hereafter VZ99) as in Paper III, to fit a purely Gaussian LOSVD from that spectrum to determine σ (this time the higher-order Gauss–Hermite moments are set to zero and are not fitted). This procedure takes into account in a precise manner the effect of the galaxy rotation on σ_e, so that no extra correction is required.

As we do not sample all galaxies out to one R_e we want to correct for this effect and to estimate how much uncertainty this can introduce in our σ_e measurements. For this we show in Fig. 2 the profiles of σ_R, measured by co-adding the SAURON spectra within circular apertures of increasing radius, for all the 40 early-type galaxies in Paper III which we sample to at least $R_e/2$. In some cases the selected circular aperture is not fully sampled by our data, and we define the radius $R \equiv \sqrt{A/\pi}$ as that of a circular aperture with the same area A on the sky actually covered by the SAURON data inside that aperture. We fitted the profile of σ_e versus R for every galaxy with a power-law relation $\sigma_R \propto R^\gamma$ and we determined the biweight (Hoaglin, Mosteller & Tukey 1983) mean and standard deviation for the exponent $\gamma = -0.066 \pm 0.035$ in the entire set. In addition we normalized the σ_R values to the corresponding $\sigma_{e/2}$, defined as the dispersion at $R_e/2$, and computed the biweight mean from all galaxies, at different fractions of R_e. This mean σ_R profile appears to be well described by the mean power-law relation fitted to the individual profiles. One can see that generally σ_R decreases by less than 5 per cent from $R_e/2$ up to R_e, but the galaxy-to-galaxy variations are significant. In summary, the aperture correction has the form:

$$\left(\frac{\sigma_R}{\sigma_e}\right) = \left(\frac{R}{R_e}\right)^{-0.066\pm0.035}.$$ (1)

The logarithmic slope of our best-fitting relation is in reasonable agreement with the value -0.04 found by Jørgensen et al. (1995) and with the value -0.06 derived by Mehlert et al. (2003) from long-slit spectroscopy.

The measured values of σ_e for our sample are given in Table 1 together with the actual fraction of R_e sampled by our kinematics. We
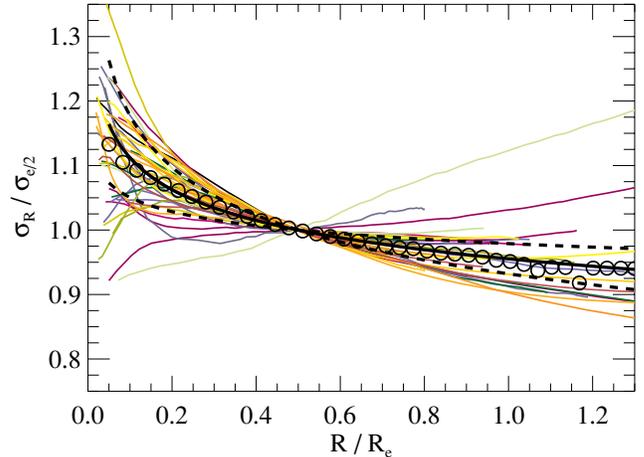
Figure 2. Luminosity-weighted second moment of the LOSVD within an aperture of radius R, normalized to its value at $R_e/2$ (see text for details). This plot shows, with the thin coloured lines, all the 40 E/S0 galaxies in the SAURON sample for which $R_e/2$ is not larger than the FOV. The open circles represent the biweight mean of all the curves at every given radius. The number of measurements sampled at every radius is not constant, moreover there are significant galaxy-to-galaxy variations in the profiles. The thick black line is a power-law relation $\sigma_R \propto R^{-0.066}$ which has an exponent defined by the biweight mean of the individual values for every galaxy. The dashed lines indicate the standard deviation in the individual slopes. The galaxy with the largest increase of the σ_R profile at large radii is NGC 4550 (see Paper III).

decided not to restrict our σ_e measurements to a smaller aperture so as not to discard data for the galaxies that we sample to large radii. In what follows we correct the values of σ_e with the aperture correction of equation (1) to determine our correlations and to generate our plots.

3 DYNAMICAL MODELLING

3.1 Multi-Gaussian Expansion mass model

We constructed photometric models for all the 29 *candidate* galaxies (see beginning of Section 2.1) plus M32 with *HST* photometry and SBF distances. For this we used the Multi-Gaussian Expansion (MGE) parametrization by Emsellem, Monnet & Bacon (1994), which describes the observed surface brightness as a sum of Gaussians, and allows the photometry to be reproduced in detail, including ellipticity variations and strongly non-elliptical isophotes. The accurate MGE modelling of such a large sample of galaxies, each consisting of three separate images, was made feasible by the use of the MGE fitting method and software by Cappellari (2002), which was designed with this kind of large-scale application in mind.

Our MGE models were fitted simultaneously to three images: (i) the WFPC2/PC1 CCD, (ii) the lower-resolution WFPC2 mosaic, and (iii) a wide-field ground-based MDM image (Fig. 3). In Section 2.2, we described how the ground-based and WFPC2 images were carefully sky-subtracted and matched. The MGE fits were done by keeping the position angle (PA) for all Gaussians fixed and taking point spread function (PSF) convolution into account (our *F*814*W* MGE PSF is given in table 3 of Cappellari et al. 2002). The quality of the resulting fits was inspected, together with the kinematics, to exclude the five galaxies which could not be reasonably well fitted by a constant-PA photometric model (Section 2.1). This reduced the original sample to 25 galaxies.
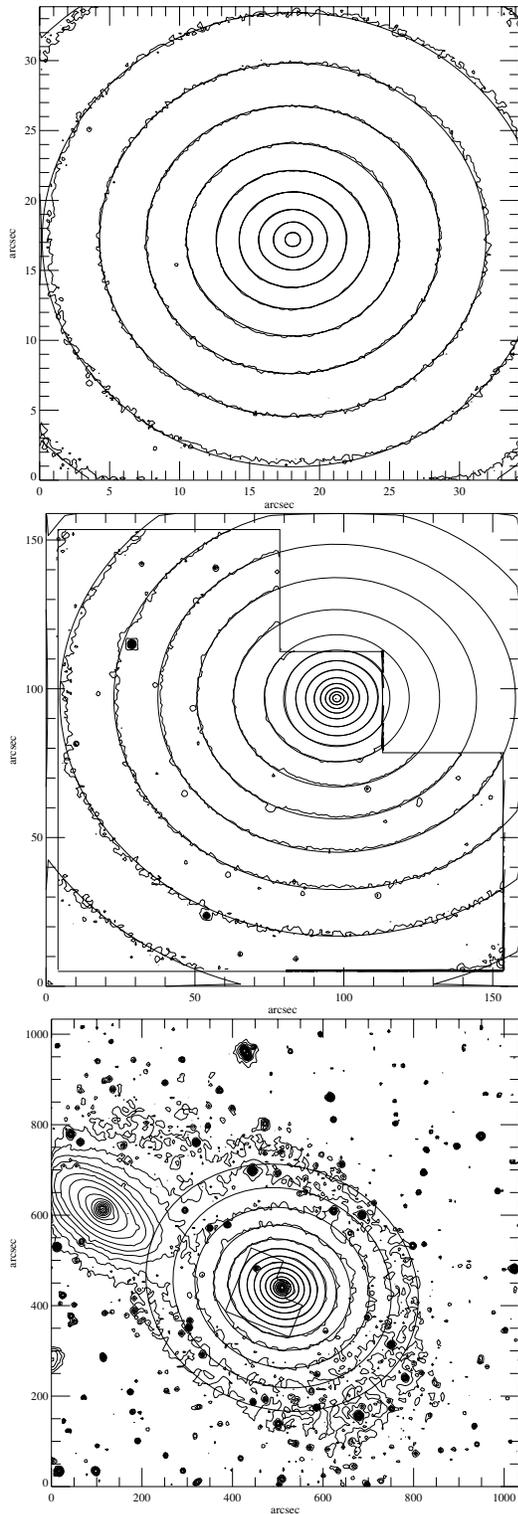
Figure 3. Contours of the surface brightness of NGC 3379 (in 0.5 mag arcsec^{-2} steps) at three different scales. Top panel: 35×35-arcsec^2 PC1 WFPC2 CCD. Middle panel: the whole 160×160-arcsec^2 WFPC2 mosaic. Bottom panel: 17.1×17.1-arcmin^2 MDM image. North is up and east is to the left-hand side. The location on the MDM field of the L-shaped WFPC2 mosaic is also shown. The galaxy at the left-hand side of the frame is NGC 3384, which was masked during the MGE fit. Superposed on the three plots are the contours of the constant-PA MGE surface brightness model, convolved with the PSF of each observation. The MGE model was fitted simultaneously to all three images.

As discussed in Cappellari (2002) we 'regularized' our solutions by requiring the axial ratio of the flattest Gaussian to be as big as possible, while still reproducing the observed photometry. In this way we avoided artificially constraining the possible inclinations for which the models can be deprojected assuming they are axisymmetric. This also prevents introducing sharp variations in the intrinsic density of the MGE model, unless they are required to fit the surface brightness. This regularization of the models is needed because of the non-uniqueness of the deprojection of an axisymmetric density distribution (Rybicki 1987).

The resulting analytically deconvolved MGE model for each galaxy was corrected for extinction following Schlegel, Finkbeiner & Davis (1998), as given by NASA/IPAC Extragalactic Database (NED). It was converted to a surface density in solar units using the WFPC2 calibration of Dolphin (2000) while assuming an *I*-band absolute magnitude for the Sun of $M_{I,\odot} = 4.08$ mag (all the absolute magnitudes of the Sun in this paper, in the *I*, *R* and *K* band, are taken from table 2.1 of Binney & Merrifield 1998). The calibrated MGE models are given in Appendix B. The MGE model for NGC 2974 was taken from Krajnović et al. (2005), which uses precisely the same method and calibration.

3.2 Two-integral Jeans modelling

We constructed axisymmetric Jeans models for the 25 galaxies in our sample in the following way. Under the assumptions of the MGE method, and for a given inclination i, the MGE surface density can be deprojected analytically (Monnet, Bacon & Emsellem 1992) to obtain the intrinsic density $\rho(R, z)$ in the galaxy meridional plane, still expressed as a sum of Gaussians. Although the deprojection is non-unique, the MGE deprojection represents a reasonable choice, which produces realistic intrinsic densities, that resemble observed galaxies when projected from any inclination.

For an axisymmetric model with constant M/L, and a stellar distribution function (DF) which depends only on two integrals of motion $f = f(E, L_z)$, where E is the energy and L_z the angular momentum with respect to the z-axis (the axis of symmetry), the second velocity moments are uniquely defined (e.g. Lynden-Bell 1962; Hunter 1977) and can be computed by solving the Poisson and Jeans equations (e.g. Satoh 1980; Binney, Davies & Illingworth 1990). The second moment μ_2 projected along the line of sight of the model is then a function of only two free parameters, i and M/L. We do not fit for the mass of a possible BH, as the spatial resolution of our data is not sufficient to constrain its value, but we set the mass of the central BH to that predicted by the $M_{\mathrm{BH}}–\sigma$ correlation (Ferrarese & Merritt 2000; Gebhardt et al. 2000) as given by Tremaine et al. (2002). The inclusion of the BH is not critical in this work, but it has a non-negligible effect for the most massive galaxies. For example, in the case of M87 the expected BH of $\sim3 \times 10^9$ M$_\odot$ produces a small but detectable effect on the observed σ up to a radius ~5 arcsec (e.g. fig. 13 of van der Marel 1994). To make our results virtually insensitive to the assumed BH masses we do not fit the innermost $R \lesssim 2$ arcsec from our data, where the BH may dominate the kinematics.

Starting from the calibrated parameters of the fitted MGE model and using the MGE formalism, the model $\mu_{2,\star}$, without a BH, can be computed easily and accurately using a single one-dimensional integral via equations (61)–(63)[1] of Emsellem et al. (1994). The contribution $\mu_{2,\bullet}$ to the second moments, due to the BH, is computed

---

[1] Their equation (63) has a typographical error and should be replaced by the following $B = \frac{1}{2}\left[\frac{e_j^2 T^4}{\sigma_j^2(1-e_j^2 T^2)} + \left(\frac{e_i}{\sigma_i q_i}\right)^2\right]$.

via equations (49), (88) and (102) of Emsellem et al. (1994) and also reduces to a single one-dimensional integral. Given the linearity of the Jeans equations with respect to the potential, the luminosity-weighted second moments for an MGE model with a BH can be obtained as $\nu_p \mu_2^2 = \nu_p \mu_{2,\star}^2 + \nu_p \mu_{2,\bullet}^2$, where ν_p is the deconvolved MGE surface brightness. The $\nu_p \mu_2^2$ has to be convolved with the PSF and integrated over the pixels before comparison with the observables. For the 25 galaxies in our sample we computed the model predictions for μ_2, at different inclinations, for each Voronoi bin on the sky. At every inclination the best-fitting M/L is obtained from the simple scaling relation $(M/L) \propto \mu_2^2$ as a linear least-squares fit:

$$(M/L) = \left(\frac{\boldsymbol{d} \cdot \boldsymbol{d}}{\boldsymbol{d} \cdot \boldsymbol{m}} \right)^2, \tag{2}$$

where the vectors $\boldsymbol{d}$ and $\boldsymbol{m}$ have elements $d_n = \mu'_{2,n}/\Delta\mu'_{2,n}$ and $m_n = \mu_{2,n}/\Delta\mu'_{2,n}$, with $\mu'_{2,n} \equiv \sqrt{V_n^2 + \sigma_n^2}$ the N measured values and $\Delta\mu'_{2,n}$ the corresponding errors, while $\mu_{2,n}$ are the model predictions for $(M/L) = 1$.

As previously noticed by other authors (e.g. van der Marel 1991) the M/L derived from Jeans modelling is only weakly dependent on inclination, due to the fact that the increased flattening of a model at low inclination ($i = 90°$ being edge-on) is compensated by a decrease of the observed velocities, due to projection effects. A quantitative explanation can be obtained by studying how the M/L determined from the tensor virial equations varies with inclination, for given observed surface brightness and μ_2. This variation for an MGE model is given by equation (77) of Emsellem et al. (1994). If the density is stratified on similar spheroids, the M/L variation is independent of the radial density profile, while only being a function of the observed axial ratio of the galaxy and the assumed inclination. A plot of the variation of M/L with inclination, for different observed axial ratios, is presented in Fig. 4 and shows that one should expect errors smaller than $\lesssim 10$ per cent even for significant errors in the inclination, if the observed galaxy has an observed axis ratio q' less than 0.7. When the galaxy is rounder than this, it is crucial to obtain a good value for the inclination, otherwise the measured M/L can be significantly in error.
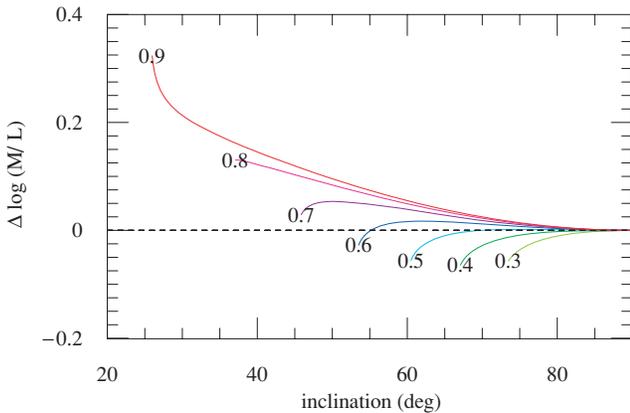
Figure 4. Relative variation of M/L predicted from the virial equations as a function of inclination, for MGE models with different constant observed axial ratios q' going from an observed flat galaxy $q' = 0.3$ (green line) to an observed round object $q' = 0.9$ (red line). At each observed axial ratio the density is assumed to be rounder than an extreme value of $q = 0.1$. Note the small variation $\lesssim 10$ per cent of the M/L estimate at different inclinations, for $q' \lesssim 0.7$.

The best-fitting inclination provided by the two-integral models need not necessarily be correct, as there is no physical reason why the real galaxies should be well described by two-integral models. None the less, we found that for the four galaxies in our sample which are not already constrained by the photometry to be nearly edge-on, and for which an independent estimate of the inclination is provided by the geometry of the dust or by the kinematics of the gas (NGC 524, NGC 2974, NGC 4150 and NGC 4459), the inclination derived from the Jeans model agrees with that indicated by the dust or gas (see Appendix A). Moreover, the round non-rotating giant elliptical galaxies (e.g. NGC 4552 and NGC 4486) are best fitted for an inclination of 90°, indicating that they are intrinsically close to spherical. This is in agreement with the fact that this whole class of massive galaxies, with flat nuclear surface-brightness profiles, which are often found at the centre of galaxy clusters, always appear nearly round on the sky and never as flattened and fast-rotating systems. They cannot all be flat systems seen nearly face-on, as the observed fraction is too high (e.g. Tremblay & Merritt 1996).

3.3 Influence of a dark matter halo

In the previous section we derived the mass density for the dynamical models by deprojecting the observed stellar photometry under the simplifying assumption of a constant M/L. In the case of spiral galaxies, for which tracers of the potential are easy to observe, a number of observational and theoretical lines of evidence suggest that, either they also contain a substantial dark matter component (see Binney 2004, for a recent review), or that a modification to the Newtonian gravity law is needed (Milgrom 1983; Bekenstein 2004). The situation is less clear regarding early-type galaxies, where it appears that in at least some galaxies dark matter is important (Carollo et al. 1995; Rix et al. 1997; Gerhard et al. 2001), while in others it may not be present at all (Romanowsky et al. 2003; Ferreras, Saha & Williams 2005). In the simple case in which the dark matter density distribution follows the stellar density, the adopted dynamical models will be correct, but the measured M/L will include the contribution of the stellar component as well as the one of the dark matter. However, in general the dark matter profile may not follow the stellar density, so the assumptions of our models could be fundamentally incorrect.

We briefly investigate the effect of a possible dark matter halo on our results using a simple galaxy model. We assume the galaxy to be spherically symmetric and the stellar density to be described by a Hernquist (1990) profile (of total mass $M = 1$), which reasonably well approximates the density of real early-type galaxies:

$$\rho_\star(r) = \frac{1}{2\pi} \frac{1}{r(r+1)^3}. \tag{3}$$

Here the density goes as $\rho_\star \propto r^{-1}$ for $r \ll 1$ and as $\rho_\star \propto r^{-4}$ for $r \gg 1$. The dark matter contribution is represented by a logarithmic potential,

$$\Phi_{\text{DM}}(r) = \frac{v_0^2}{2} \ln \left(r^2 + r_0^2 \right), \tag{4}$$

which is the simplest potential producing a flat circular velocity v_0 at large radii ($r \gg r_0$), as observed in real galaxies.

With these assumptions, the projected second moment μ_2 of an isotropic model, which is equal to the projected velocity dispersion σ_p due to the spherical symmetry, is given, for example, by equation (29) of Tremaine et al. (1994). Substituting the adopted expressions,

we obtain:

$$\sigma_p^2(R) = \frac{1}{\pi \Upsilon I(R)}$$
$$\times \int_R^\infty \left[\frac{1}{r(r+1)^2} + \frac{v_0^2}{(r^2 + r_0^2)} \right] \frac{\sqrt{r^2 - R^2}}{(r+1)^3} \, dr, \qquad (5)$$

where $I(R)$ is the stellar surface brightness at the projected radius R, Υ is the stellar M/L, and we assumed a gravitational constant $G = 1$. This integral can be evaluated analytically [$I(R)$ is given in Hernquist (1990)], but it is trivially computed numerically.

The results from this formula, evaluated for four different values of $v_0 = 0, \ldots, v_{0,\max}$, are shown in the middle panel of Fig. 5. The
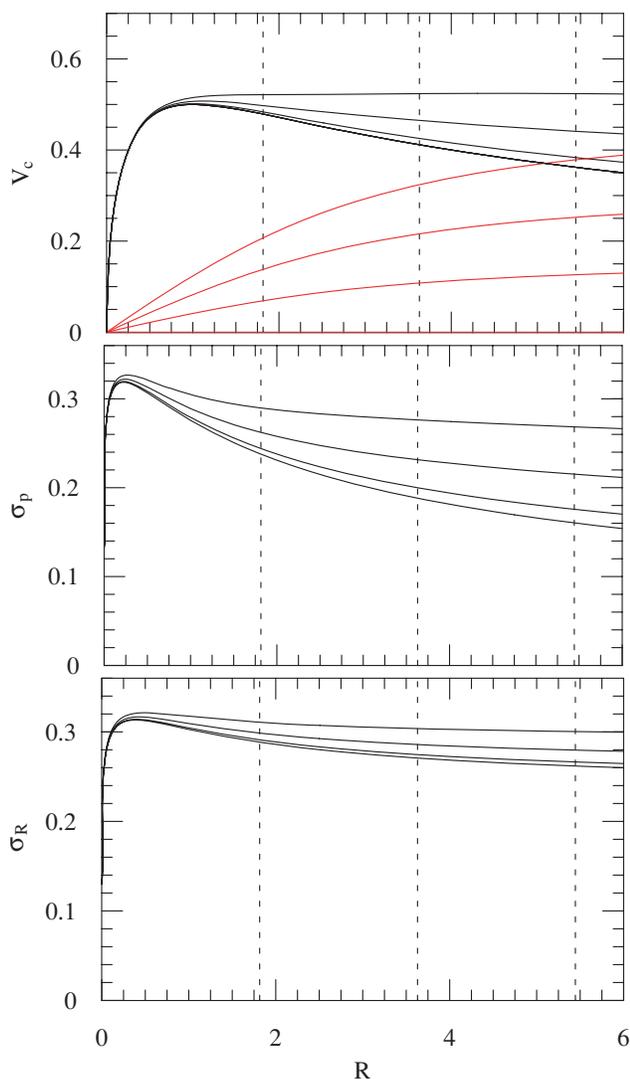
Figure 5. Top panel: black lines, from bottom to top, circular velocity v_c, as a function of radius R, of a spherical Hernquist galaxy model, with a dark halo described by a logarithmic potential, for four different values of the asymptotic halo velocity $v_0 = 0$, 0.15, 0.30 and 0.45. The contribution to the circular velocity of the dark halo component alone is shown with the red lines. The three vertical dashed lines indicate the position of 1, 2 and 3 half-light radii of the model. Middle panel: projected velocity dispersion σ_p for the same four models shown in the top panel. The lowest curve is the Hernquist model without a dark halo ($v_0 = 0$). Bottom panel: same as in the middle panel, for the luminosity-weighted aperture velocity dispersion σ_R. This is the same quantity which is plotted in Fig. 2 for the real galaxies.

characteristic radius $r_0 = 3.5$ of the dark halo and the value of $v_{0,\max} = 0.45$ were chosen so as to make the circular velocity v_c of the stellar plus dark matter component as constant as possible in the range $R = 1.815$–5.446 (top panel of Fig. 5), which corresponds to 1–3 half-light radii R_e. This simple choice tries to mimic the typical observations of real early-type galaxies (e.g. fig. 2 of Gerhard et al. 2001). Under these assumptions the dark matter represents 16 per cent of the total mass inside R_e and 52 per cent inside $3R_e$. These values are roughly consistent with the values reported by Gerhard et al. (2001) for real galaxies.

For this simple model, and assuming the largest dark matter contribution, the projected velocity dispersion σ_p is increased by 22 per cent at R_e (the typical maximum radius sampled by our SAURON kinematics) and by 9 per cent at $R_e/2$, with respect to a model without dark halo. The luminosity-weighted velocity dispersion inside a circular aperture σ_R is increased by 8 per cent inside R_e and by 4 per cent inside $R_e/2$ (bottom panel of Fig. 5).

To get an indication of the overestimation of the stellar M/L we would obtain by fitting constant M/L models to galaxies with dark haloes, we logarithmically rebinned the σ_p profile of the model with dark halo (to mimic the spatial sampling of the real data), and fitted to it the model without dark halo, in the radial range 0–R_e. We obtained that the true stellar M/L would be overestimated by $\sim$12 per cent, in the case of maximum dark halo. This shows that, under these hypotheses, the dark matter would start producing small but measurable variations in the global M/L.

3.4 Three-integral dynamical modelling

As we mentioned in the Introduction, part of the observed FP tilt could come from non-homology in the orbital distribution of galaxies, as a function of luminosity. To test if this is the case, we compared the M/L derived using the quicker and simpler two-integral Jeans models, with general stationary and axisymmetric three-integral dynamical models.

The three-integral dynamical modelling we adopted is based on Schwarzschild's (1979) numerical orbit-superposition method, which is able to fit all kinematic and photometric observations (Richstone & Tremaine 1988; Rix et al. 1997; van der Marel et al. 1998). A similar approach was adopted by us and by other groups to measure the BH masses in galaxy nuclei or to analyse the stellar orbital distribution (e.g. Cretton et al. 1999; Cappellari et al. 2002; Verolme et al. 2002; Gebhardt et al. 2003; Thomas et al. 2004; Valluri, Merritt & Emsellem 2004). The method provides a general description of axisymmetric galaxies, its stronger assumption being that of the stationarity of the galaxy potential. In practice, the method only requires the potential not to vary on the time-scale required to sample the density distribution of an orbit. As the dynamical time-scale in ellipticals is of the order of a few 10^7 yr at R_e, while galaxy evolution generally happens on much longer time-scales, this assumption is expected to be valid in the regions that we sample with our kinematics.

In our implementation of the Schwarzschild method we use the MGE parametrization to describe the stellar density and to calculate the gravitational potential, as in Cappellari et al. (2002) and Verolme et al. (2002). However, we use here a new code which was specifically designed with the improved quality of our input integral-field kinematical data in mind. We verified that the new code produces the same results as the old one (within the numerical approximations of the method), when identical conditions are adopted. The key updates to the modelling method, with respect to the description given in van der Marel et al. (1998) and in Cappellari et al. (2002), consist of the following.
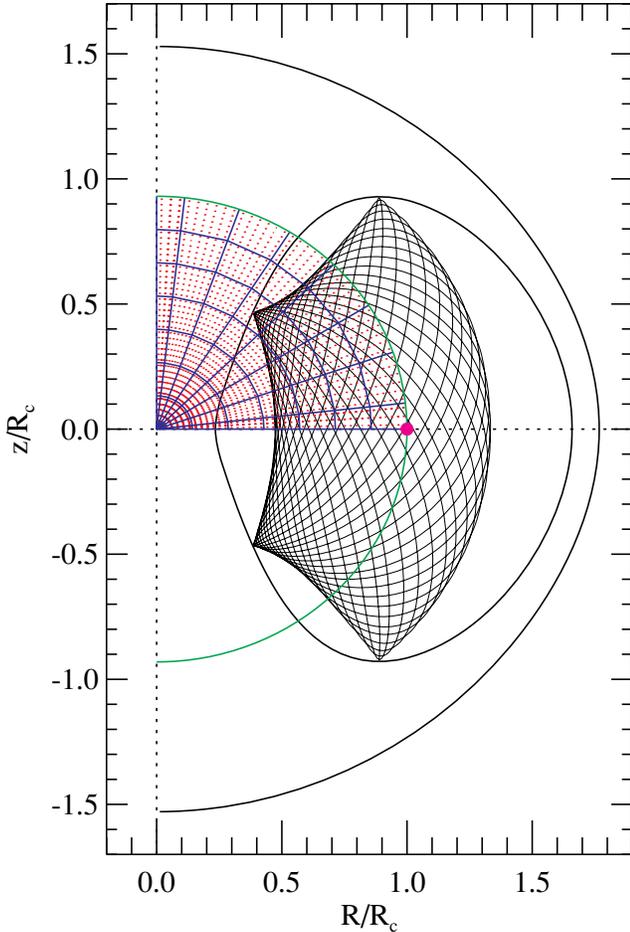
Figure 6. Visualization of our orbital starting scheme and dithering at a given energy E in the meridional plane (R, z) of an axisymmetric galaxy (cf. fig. 5 of van der Marel et al. 1998). The large magenta dot marks the location of the circular orbit. At each E we start orbits from the meridional plane with $v_R = v_z = 0$ and $L_z > 0$, with initial coordinates arranged in a polar grid, linear in the eccentric anomaly and in radius (small red dots), going from $R = z = 0$, to the curve defined by the locus (green line) of the thin tube orbits, to reduce duplications. We then construct 'dithered' orbital bundles by grouping together (blue lines) every adjacent set of N_{dither}^3 orbits and co-adding them before computing the observables (at one E one can only visualize N_{dither}^2 points or 6×6 in this plot). The first and last angular sectors have half size, to provide a uniform angular sampling across the R and z axes (considering the bi-symmetry of the model). Also shown is a representative regular non-resonant orbit, started near the centre of one orbital bundle, enclosed in its zero-velocity curve. The outermost black solid line is the equipotential, which includes every orbit at the given E.

(i) The orbit library required by the method has to be sampled by choosing the starting points of the orbits so as to cover a three-dimensional space defined by the isolating integrals of motion, the energy E, the z-component of the angular momentum L_z and the third integral I_3. In previous works, at each E, we sampled orbits linearly in L_z, and for each (E, L_z) pair, an angle was used to parametrize I_3 (see fig. 5 of van der Marel et al. 1998). Here at each E we start orbits from the meridional plane with $v_R = v_z = 0$ and $L_z > 0$ with positive initial coordinates arranged in a polar grid (linear in eccentric anomaly and in radius) going from $R = z = 0$, to the curve defined by the locus of the thin tube orbits (Fig. 6), to reduce duplications. The reason for our change is that we want

to sample observable space as uniformly as possible, as opposed to sample the space of the integrals of motion, which is not directly observable. With the new scheme the cusp singularities, which characterize the observables of orbits (see fig. 1.2 of Cappellari et al. 2004) are distributed evenly on the sky plane.

(ii) Ideally, the orbit library in Schwarzschild's method should provide a complete set of basis functions for the DF. Individual orbits correspond to DFs that are δ-functions and an infinite number of them can indeed represent any smooth DF. However, only a limited number of orbits can be used in real models, which then have a non-smooth DF and generate unrealistically non-smooth observables. To alleviate this problem, instead of using single orbits as basis functions for the DF in the models, we use 'dithered' orbital components, constructed by co-adding a large bundle of orbits started from different but adjacent initial conditions. The starting points are arranged in such a way that the (regular) orbits differ in all three integrals of motion (Fig. 6). This technique produces smoother components, which are also more representative of the space of integrals of motions they are meant to describe [a similar approach was used for spherical models by Richstone & Tremaine (1988) and Rix et al. (1997)]. With dithered orbits we can construct models which better approximate real galaxies than would otherwise be possible with single orbits, due to computational limitation. Dithering is crucial for this work, as otherwise the numerical noise generated by the relatively small orbit number would limit the accuracy in the determination of the M/L.

(iii) We do *not* use Fourier convolutions to model PSF effects. Given that the computation of the orbital observables is intrinsically a Monte Carlo integration, we also deal with the PSF in the same way. The phase-space coordinates are computed at equal time-steps during the orbit integration (using the DOP853 routine by Hairer, Norsett & Wanner 1993). They are projected on the sky plane, generating the triplets of values (x', y', v_z'), which are regarded as 'photons' coming from the galaxy. The sky coordinates (x', y') of each photon are randomly perturbed, with probability described by the MGE PSF, before being recorded directly into any of the observational apertures. In this way no interpolation or intermediate grids are required and the accuracy of the computation of the observables is only determined by the (large) number of photons generated. Voronoi two-dimensional binning is treated in the model in the same way as in the observed data (Section 2.3).

For the sampling of the orbit library in the present paper we adopted a grid of 21 energies, and at every energy we used eight angular and seven radial sectors, with $N_{dither} = 6$ (as in Fig. 6). This means that the final galaxy model is made of $21 \times (8 - 1) \times 7 \times 2 \times 6^3 = 444\,528$ different orbits, which are bundled in groups of $6^3 = 216$ before the linear orbital superposition. From each orbital component we generate $\sim 2 \times 10^8$ 'photons' on the sky plane, which are used for an accurate Monte Carlo calculation of the observables inside the Voronoi bins. At each bin position we fit V, σ and four Gauss–Hermite parameters up to h_6.

Some of the models whose M/L we use in this paper were already presented elsewhere. An application of this new code to the modelling of the two-dimensional binned kinematics of the elliptical galaxy NGC 4473, which contains two counter-rotating spheroids, and a study of the orbital distribution of the giant elliptical galaxy M87 was presented in Cappellari & McDermid (2005). The modelling of the elliptical galaxy NGC 2974, and detailed tests of the ability of this orbital sampling scheme to recover a given M/L and a realistic DF are presented in Krajnović et al. (2005).

In contrast to studies of spiral galaxies, where the inclination can be inferred from the observed geometry of the disc, there is usually no obvious way to infer the inclination of early-type galaxies, and it therefore is one of the free parameters of the models. Krajnović et al. (2005) showed that there is evidence for the inclination to be possibly degenerate using axisymmetric three-integral models, even if the LOSVD is known at every position on the projected image of the galaxy on the sky. Here we confirmed this result using a larger sample of galaxies, in the sense that the models are generally able to fit the observations within the measurement errors, for wide ranges of variation in inclination. For these reasons we fitted the M/L by constructing sequences of models with varying M/L, while keeping the inclination fixed to the best-fitting value provided by the Jeans models (Table 1). We show in Appendix A that the inclination derived from the Jeans models may be more accurate than just assuming all galaxies are edge-on, although we are aware it may not always be correct. In any case, we have shown in Fig. 4 that the results of this work do not depend critically on the assumed inclination.

The Schwarzschild models use the same MGE parameters as the Jeans models (Section 3.2) and also include a central BH as predicted by the M_{BH}–σ relation. More details on the modelling and the motivation of the changes, together with a full analysis of the orbital distribution inferred from the models are given in a follow-up paper. The fact that the models can generally fit the observed density and the SAURON integral-field kinematics of our galaxies with a constant M/L seems to confirm the suggestion of Section 3.3: either mass follows light in galaxy centres, or we cannot place useful constraints on the dark matter halo from these data. This may be explained by the existence of an intrinsic degeneracy in the simultaneous recovery of the potential and the orbital distribution from the observed LOSVD, as discussed, for example, in section 3 of Valluri et al. (2004), combined with the relatively limited spatial coverage. In a few galaxies the h_4 and h_6 Gauss–Hermite moments cannot be reproduced in detail by our models and may be improved, for example, by allowing the M/L to vary or extending to triaxial geometry.

4 RESULTS

4.1 Comparing M/L of two- and three-integral models

In this section, we compare the measurements of M/L obtained with the two-integral Jeans models described in Section 3.2 with the results obtained with the more general Schwarzschild models of Section 3.4. The usefulness of this comparison comes from the fact that the Jeans models are not general, but can be computed to nearly machine numerical accuracy, so they will generally provide biased results, but with negligible numerical noise. The Schwarzschild models are general, within the assumptions of stationarity and axisymmetry, but are affected by numerical noise and can be influenced by a number of implementation details. A comparison between these two substantially different modelling methods will provide a robust estimate of the uncertainties in the derived M/L, including systematic effects. The best-fitting correlation (Fig. 7) shows a small systematic trend $(M/L)_{Schw} \propto (M/L)_{Jeans}^{1.13\pm0.05}$, while the scatter in the relation indicates an intrinsic error of 6 per cent in the models. Formal errors in the Schwarzschild M/L are generally not too different from this more robust estimate (e.g. Krajnović et al. 2005).

One can see in Fig. 7 that the galaxies with the highest M/L tend to show an $(M/L)_{Schw}$ which is systematically higher than $(M/L)_{Jeans}$
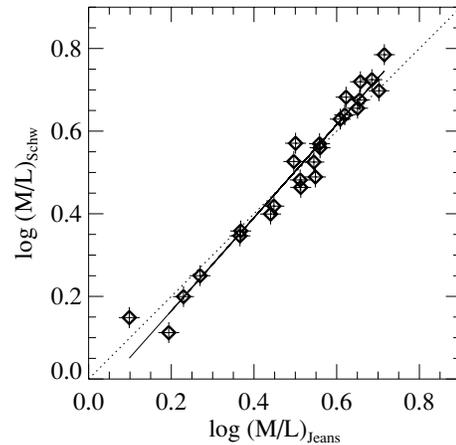
Figure 7. Comparison between the 25 M/L determinations using the two-integral Jeans dynamical models and the three-integral Schwarzschild models. An error of 6 per cent in the model accuracy is required to explain the observed scatter along the best-fitting relation (solid line). The dotted line represents a one-to-one relation.

(see also Table 1). The difference in the M/L is likely due mainly to the fact that the Schwarzschild models use the full information on the LOSVD, while the Jeans models are restricted to the first two moments. For this reason, in the following sections, unless otherwise indicated, we will use the term 'dynamical M/L', or simply M/L, to refer to the $(M/L)_{Schw}$, which is expected to provide a less-biased estimate of the true M/L.

4.2 Observed correlations

The data consist of $N = 25$ estimates of the dynamical M/L in the I band and corresponding measurements of the luminosity-weighted second moment of the LOSVD σ_e within the half-light radius. We fitted a linear relation of the form $y = \alpha + \beta x$, with $x = \log(\sigma/\sigma_0)$ and $y = \log(M/L)$, and minimizing

$$\chi^2 = \sum_{j=1}^{N} \frac{(y_j - \alpha - \beta x_j)^2}{(\Delta y_j)^2 + \beta^2 (\Delta x_j)^2}, \qquad (6)$$

with symmetric errors Δx_j and Δy_j, using the FITEXY routine taken from the IDL[2] Astro-Library (Landsman 1993), which is based on a similar routine by Press et al. (1992). This is the same approach adopted by Tremaine et al. (2002) to measure the slope of the correlation between the mass M_{BH} of the central BH and σ_e, and we refer to that paper for a comparison of the relative merits of alternative methods. The M/L measurements are inversely proportional to the assumed distance, which is taken from Tonry et al. (2001) and was adjusted to the new Cepheids zero-point of Freedman et al. (2001) by *subtracting* 0.06 mag from the SBF distance moduli (Table 1). For this reason the errors in the distance represent a lower limit to the errors in M/L. In the fit, we assigned to the M/L the distance errors quadratically co-added to the 6 per cent modelling error derived in Section 4.1. The σ_e values are measured from spectra of extremely high S/N, and have negligible statistical errors, but their accuracy is limited by template mismatch and possible calibration accuracy. We adopted an error in σ_e of 5 per cent. An upper limit to the error in σ_e can be derived by comparing our values with the central σ_c in published data (HyperLeda;[3] Prugniel & Simien 1996), which is closely

---

[2] http://www.rsinc.com/idl
[3] http://leda.univ-lyon1.fr/
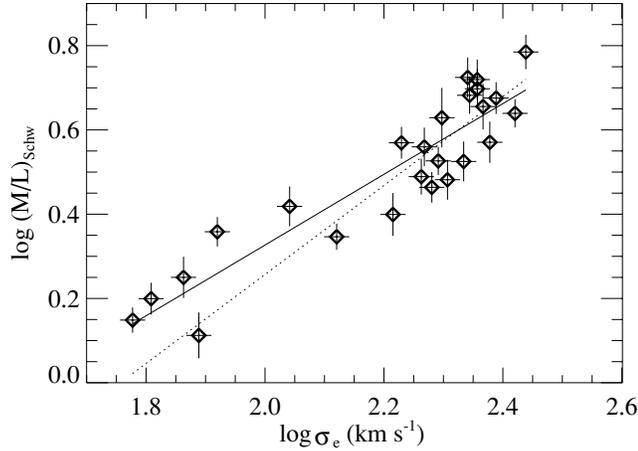
Figure 8. (M/L)–σ_e correlation. The errors in the M/L values shown here and in the following plots represent the uncertainty in the distance as given by Tonry et al. (2001), quadratically co-added to the 6 per cent modelling error determined in Section 4.1. The errors on σ_e are assumed to be 5 per cent. The solid line is the correlation obtained by fitting all galaxies, while the dotted line is the fit obtained by excluding the five galaxies with $\log \sigma_e < 2$. The galaxy with the smallest σ_e is M32.

related to our σ_e, but it is measured in a very different way. We found that errors of 7 per cent in σ are needed to explain the scatter with respect to a linear relation between $\log \sigma_c$ and $\log \sigma_e$. This scatter also includes very significant systematics due to the differences in the data, analysis and measurement method. The adopted 5 per cent error provides a conservative estimate of the true errors. Note that for the galaxy M87 our σ_e value is 20 per cent smaller than the value adopted by Tremaine et al. (2002). Our SAURON kinematics, however, agrees well with both the *G*-band and the Ca triplet stellar kinematics by van der Marel (1994). Adopting our smaller σ_e M87 would become an outlier of the M_{BH}–σ_e correlation.

We find a tight correlation (Fig. 8) with an *observed* rms scatter in M/L of 18 per cent. The best-fitting relation is

$$(M/L) = (3.80 \pm 0.14)\left(\frac{\sigma_e}{200 \text{ km s}^{-1}}\right)^{0.84\pm0.07}. \tag{7}$$

The value of $\sigma_0 = 200$ km s^{-1} was chosen, following Tremaine et al. (2002), to minimize the uncertainty in α and the correlation between α and β. The best-fitting values and the uncertainties, here as in all the following correlations, were determined after increasing the errors Δy_j in the M/L by quadratically co-adding a constant 'intrinsic' scatter so that $(\Delta y_j)^2$ is replaced by $(\Delta y_j)^2 + (\Delta y_0)^2$, to make $\chi^2/\nu = 1$, where $\nu = N - 2 = 23$ is the number of degrees of freedom in the linear fit (see, Tremaine et al. 2002, for a discussion of the approach). The constant intrinsic scatter implied by the observed scatter in this correlation is $\sim$13 per cent ($\Delta y_0 = 0.053$).

To test the robustness of the slope we also performed a fit only to the galaxies with $\log \sigma_e > 2$, which is the range most densely sampled by FP studies (e.g. Jørgensen et al. 1996). The relation becomes in this case $(M/L) \propto \sigma_e^{1.06\pm0.18}$, which is steeper, but is still consistent with equation (7) within the much larger uncertainty. The steepening of the correlation at high σ_e may also be due to a non-perfect linearity of the relation (e.g. Zaritsky, Gonzalez & Zabludoff 2005), but this cannot be tested with our limited number of galaxies. The correlation computed using the Jeans determinations is even tighter than equation (7), and gives $(M/L)_{Jeans} \propto \sigma_e^{0.77\pm0.06}$ with an observed scatter of only 15 per cent. However, due to the possi-

ble bias of the Jeans M/L values, we will use the Schwarzschild determinations in what follows.

The use of σ_e determined from integral-field data and using a large aperture has the significant advantage that it is conceptually rigorous and accurate. However, the (M/L)–σ correlation does not appear to depend very strongly on the details by which σ is determined. We performed the same fit of Fig. 8 using as value of the dispersion the $\sigma_{e/8}$ measured from the SAURON data in an aperture of radius $R_e/8$. In this case the best-fitting correlation has the form $(M/L) \propto \sigma_{e/8}^{0.75\pm0.06}$ and the observed rms scatter in M/L is 21 per cent. As an extreme test we used as dispersion the inhomogeneous set of central values σ_c, obtained from long-slit spectroscopic observations, as given in the HyperLeda catalogue. In this case the best-fitting correlation becomes $(M/L) \propto \sigma_c^{0.87\pm0.07}$ and has an observed scatter of 20 per cent. Both correlations are consistent within the errors with the best-fitting (M/L)–σ_e correlation, although they have a larger scatter.

We also determined the correlation between the M/L and the second moment of the velocity, corrected with equation (18) of van der Marel & Franx (1993)

$$\tilde{\sigma}_e \approx \sigma_e(1 + h_{4,e}\sqrt{6}), \tag{8}$$

to include the contribution to the second moment of a non-zero $h_{4,e}$ parameter. Equation (8) was obtained by integrating the LOSVD to infinite velocities. In practice the second moment of a parametrized LOSVD with dispersion σ and $h_4 = 0.1$ is equal to $\tilde{\sigma} = 1, 1.11$ and 1.21σ if one sets the LOSVD to zero for velocities larger than $|V| > 2.45, 3$ and 4σ, respectively. This shows that the correction has to be used with care, being highly sensitive to the details of the LOSVD at large velocities, where the LOSVD cannot be determined reliably. In fact a measured positive h_4 parameter, which means the LOSVD is narrower than a Gaussian at small velocities, does not necessarily imply that the wings of the LOSVD are precisely as described by the Gauss–Hermite parametrization. We find a correlation consistent, within the errors, with equation (7) and with comparable scatter.

We also studied the correlation of the dynamical M/L with the galaxy luminosity (Fig. 9). For this we used our own total magnitudes in the *I*-band I_T given in Table 1, transformed into absolute
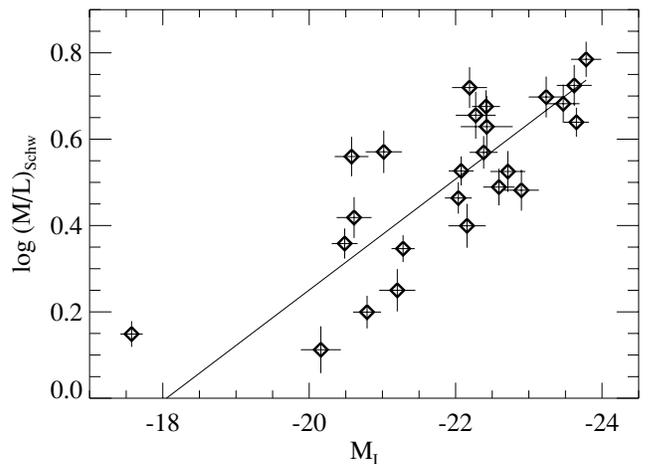
Figure 9. (M/L)–L_I correlation. Note that all galaxies, with the exception of M32 are brighter than the limit $M_I \approx -20$ mag, in absolute magnitudes, which is set by the luminosity-selection criterion of the SAURON survey. Due to the sensitivity of the fit to the single M/L of M32, this galaxy was not included in this and in the following fits involving luminosity or mass, but it is included in the plots, to allow a comparison with Fig. 8.

magnitudes using the SBF distances and the galactic absorption (Schlegel et al. 1998) given in Table 1. The I_T measurements are dominated by possible systematic errors due to the extrapolation involved and the possible contamination by nearby objects. To obtain a realistic estimate of the errors we compared our I_T with the same value[4] measured by Tonry et al. (2001) in the same photometric band. A fit to the two sets of values showed no systematic trend with magnitude and a zero-point shift of 0.09 mag. The observed scatter is consistent with errors of 13 per cent in each measurement, and we assigned this error to our I_T values. A stringent internal test on the errors in the I_T measurements comes from the comparisons with the total luminosities obtained by co-adding all the Gaussians of the MGE models of Section 3.1. A correlation of the two quantities shows no deviant points and no systematic trend in either slope or zero-point, and is fully explained by an 8 per cent random error in both quantities. This estimate is similar to the typical measurement errors of 9 per cent reported by Jørgensen et al. (1996). We also compared I_T with the corresponding values of B_T in the B band as given by the HyperLeda catalogue (Prugniel & Simien 1996). We found a smooth variation of the $B - I$ colour with luminosity, consistent with the quoted measurement errors in this quantity and indicating the absence of significant systematic errors or any deviant point. The fit was performed in the same way as above and provided the relation:

$$(M/L) = (2.35 \pm 0.19) \left(\frac{L_I}{10^{10} L_{I,\odot}} \right)^{0.32 \pm 0.06}. \quad (9)$$

This correlation has an observed rms scatter in M/L of 31 per cent which is much larger than that of the correlation (7). In particular there is a significant scatter for the eight galaxies in the luminosity range $-21.5 \lesssim M_I \lesssim -19.5$ mag. Given the fact that all galaxies in the SAURON sample were selected to have $M_B \leqslant -18$ mag, which translates in the I band into $M_I \lesssim -20$ mag, the fit depends very sensitively on the single M/L of M32, which also has a small distance error. Moreover, there is some indication that the dwarf E galaxies like M32 may populate a different FP from the normal E galaxies (Burstein et al. 1997; but see Graham & Guzmán 2003). For these reasons we excluded M32 from this fit and all the following fits involving luminosity or mass.

4.3 Understanding the tightness of the correlations

The decrease of the scatter in M/L, when going from the (M/L)–L correlation to the (M/L)–σ one is reminiscent of what happens to the similar correlations involving the BH mass M_{BH} instead of the M/L. This decrease of the scatter shows that at a given galaxy luminosity the M/L is higher when the σ is higher. One may apply the arguments used to understand the tightness of the M_{BH}–σ relation (Ferrarese & Merritt 2000; Gebhardt et al. 2000) to the (M/L)–σ relation as well. There can be two main reasons for the (M/L)–σ relation to be tighter than the (M/L)–L relation: (i) the M/L may correlate with galaxy mass, but the luminosity may not be a good mass estimator, due to differences of M/L at a given luminosity; in this case variations of σ would reflect variations of M/L; (ii) the M/L may be related to the galaxy compactness, which implies a higher σ at a given mass. In the case of the M_{BH}–σ relation both effects seem to play a role: Kormendy & Gebhardt (2001) showed that the galaxies with higher σ are indeed more compact than average (see also Graham et al. 2001). Subsequently, Marconi & Hunt

---

[4] $I_T = \bar{m}_I - \bar{N}_I$ in the notations of table 1 of Tonry et al. (2001).
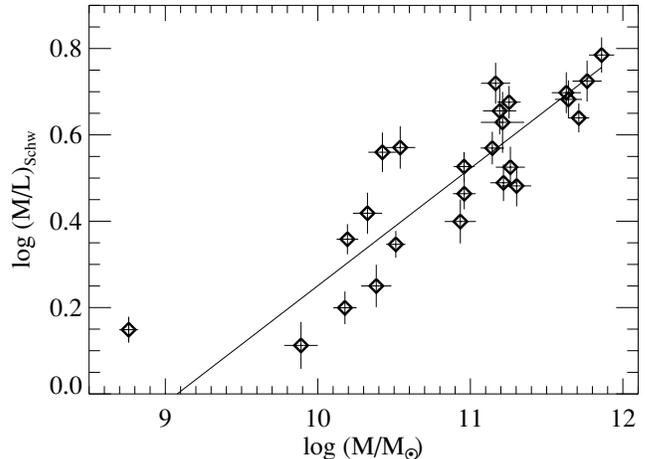
Figure 10. (M/L)–M correlation. Here the I-band luminosity of each galaxy was converted into mass by multiplication by its M/L. The least massive galaxy is M32, and was not included in the fit.

(2003) and Häring & Rix (2004) showed that much tighter correlations for M_{BH} are obtained using the galaxy mass instead of the luminosity.

It is clear from Fig. 9 that there is a spread in M/L at a given galaxy luminosity, so the first argument above must play a role in tightening the correlation. To test the importance of this effect we verify how much better the M/L correlates with galaxy mass after multiplying each luminosity by its measured M/L. The best-fitting correlation (Fig. 10) is given by

$$(M/L) = (1.78 \pm 0.16) \left(\frac{M}{10^{10} \, \mathrm{M}_\odot} \right)^{0.27 \pm 0.03}. \quad (10)$$

This correlation has an observed scatter in M/L of 24 per cent. It is tighter than the (M/L)–L correlation, but still significantly less tight than the (M/L)–σ one.

An alternative way to verify the importance of the M/L variations in increasing the scatter of the (M/L)–L relation is to use the galaxy luminosity in the near-infrared, instead of in the I band. The near-infrared better samples the light emitted by the bulk of the galaxies' old stellar population. Moreover in that wavelength range the M/L variations with mass are smaller (e.g. Bell & de Jong 2001). These are apparently the reasons why Marconi & Hunt (2003) found a much tighter M_{BH}–L correlation in the K band than in the B band.

We want to see if the same tightening happens in our case with the M/L. The correlation between the I-band M/L and the K-band luminosity, extracted from the Two-Micron All-Sky Survey (2MASS) Extended Source Catalogue (XSC; Jarrett et al. 2000), is shown in Fig. 11. We adopted the same constant error of 13 per cent in the luminosity, as we used in the I band, instead of the errors given in the XSC, which have an unrealistically small median value of 2 per cent. The best-fitting relation is nearly identical to equation (9) having the form

$$(M/L) = (1.88 \pm 0.20) \left(\frac{L_K}{10^{10} L_{K,\odot}} \right)^{0.32 \pm 0.05}, \quad (11)$$

adopting $M_{K,\odot} = 3.28$ mag. This relation has indeed a slightly smaller rms scatter in M/L, of 28 per cent, than the I-band correlation.

Finally, to test the importance of the second argument above, namely, the effect of the galaxy compactness in tightening our (M/L)–σ correlation, we show in Fig. 12 the same (M/L)–L
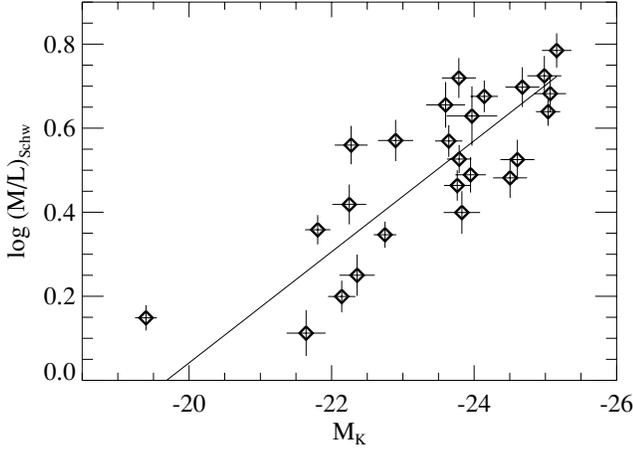
Figure 11. (M/L)–L_K correlation. Same as in Fig. 9, but here the M/L is plotted against the 2MASS galaxy absolute magnitude in the K band. The faintest galaxy is M32 which was not included in the fit.
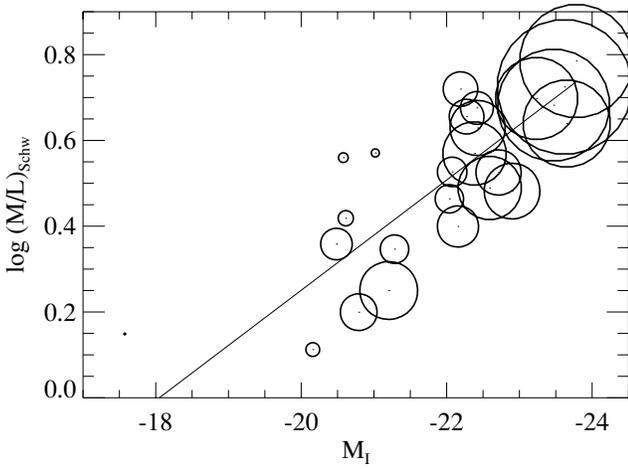
Figure 12. (M/L)–L_I correlation as in Fig. 9. The radius of the circles, centred around each measurement, is proportional to the galaxy R_e in pc.

relation as in Fig. 9, but we also overplot the effective radii R_e of the galaxies (in pc). The eight galaxies with $-21.5 \lesssim M_I \lesssim -19.5$ mag differ substantially in their R_e. Indeed the galaxies with higher M/L are also the most compact at a given luminosity. This explains why they also have the highest σ (see, Kormendy & Gebhardt 2001 for a discussion), and it shows why, at least for our limited galaxy sample, the (M/L)–σ correlation is even tighter than the (M/L)–M relation.

To summarize the results of this section, we found that (i) the tightest correlation is the (M/L)–σ relation, followed by (M/L)–M and (M/L)–L_K. The (M/L)–L_I relation is the least tight. This sequence of increasing scatter suggests that the M/L correlates primarily with galaxy mass, and at given mass, with galaxy compactness. However, we caution the reader that the size of our sample is too small to draw definitive conclusions. In fact, with the exception of the (M/L)–σ relation, the difference in scatter between the different correlations is only at a few sigma level. A larger sample is needed to make this result stronger.

4.4 Understanding the tilt of the FP

The existence of the FP of the form $R_e \propto \sigma^\alpha I_e^\beta$, combined with the homology and virial equilibrium assumption $M \propto \sigma^2 R_e$ and the

geometric definition $L \propto I_e R_e^2$, yields a prediction for the $(M/L)_{FP}$ (Dressler et al. 1987; Faber et al. 1987). Here we adopt an FP of the form:

$$R_e \propto \sigma^{1.24\pm0.07} I_e^{-0.82\pm0.02}, \quad (12)$$

as determined in the Gunn r band by Jørgensen et al. (1996) from a sample of 225 early-type galaxies in nearby clusters. We choose these numerical values because the photometric parameters R_e and I_e for this FP were measured from a homogeneous sample of E and S0 galaxies, in the same way as we did (Section 2.2). This FP determination agrees within the errors with other determinations in similar photometric bands (see Colless et al. 2001, and references therein) and also with the I-band determination by Scodeggio, Giovanelli & Haynes (1997), so the choice of the FP coefficients is not critical. One important exception is the FP determination by Bernardi et al. (2003), derived from a large sample of galaxies from the Sloan Digital Sky Survey. The parameters of that FP are inconsistent with most previous determinations, and the reason for this discrepancy is currently unclear. Considering also that their photometric parameters were derived by fitting the galaxy profiles and not from a growth curve, as in this and other FP works, we decided not to consider their values here. Taking the numerical values by Jørgensen et al. (1996), one can derive the following relations for the $(M/L)_{FP}$, as a function of the combination $R_e \sigma$ or equivalently galaxy mass, and galaxy luminosity:

$$\begin{aligned}(M/L)_{FP} &\propto R_e^{-1-1/\beta}\sigma^{2+\alpha/\beta} \\ &= R_e^{0.22\pm0.03}\sigma^{0.49\pm0.09} \\ &\propto R_e^{-(2+\alpha)/(2\beta)-2}M^{1+\alpha/(2\beta)} \\ &= R_e^{-0.02\pm0.06}M^{0.24\pm0.05}, \quad (13)\end{aligned}$$

$$\begin{aligned}(M/L)_{FP} &\propto I_e^{-1/2-(1+2\beta)/\alpha}L^{-1/2+1/\alpha} \\ &= I_e^{0.02\pm0.04}L^{0.31\pm0.05}. \quad (14)\end{aligned}$$

The scatter in the relations amounts to 23 per cent between M/L and $R_e^{0.22}\sigma^{0.49}$ or mass, and 31 per cent between M/L and L. Within the errors the $(M/L)_{FP}$ can be written as a simple power law of either luminosity or mass alone. This simple dependence is what is usually known as the 'tilt' of the FP. The $(M/L)_{FP}$ cannot be written explicitly as a simple function of σ; however, Jørgensen et al. (1996) note that 'the inclusion of R_e is not even essential' as a direct correlation between $(M/L)_{FP}$ and σ gives a correlation:

$$(M/L)_{FP} \propto \sigma^{0.86}, \quad (15)$$

with an observed scatter virtually unchanged of 25 per cent.

As mentioned before, the correctness of the FP prediction for the M/L depends on the homology assumption, regarding both the surface brightness and the orbital distribution of early-type galaxies (e.g. Ciotti et al. 1996). Our dynamical M/L is based on detailed photometric models, so it is independent of the spatial homology assumption. Moreover, we include the full LOSVD to estimate the M/L and we do not need to make any extra correction for galaxy rotation. Finally, the good agreement between the M/L derived with two-integral Jeans and three-integral Schwarzschild models shows that orbital non-homology does not have an important effect on the M/L (Section 4.1). We are thus in the position to compare directly our M/L determinations, which do not depend on any homology assumption, with the homology-dependent $(M/L)_{FP}$.

Comparison between the FP tilt given by equation (14) and relation (9) shows that the dependence of the dynamical M/L on luminosity is the same. Taking the measurement errors into account this indicates that non-homology cannot produce more than

~15 per cent of the observed tilt. For the more reliable correlations involving σ, comparison of the virial prediction of equation (15) and the modelling result of equation (7) indicates that non-homology can account for at most ~7 per cent of the tilt. Both relations consistently imply that the FP tilt reflects essentially a real variation of the total M/L in the central regions of galaxies, which can be due to variations in the galaxies' stellar population and/or in the dark matter fraction. A similar conclusion was reached by Lanzoni et al. (2004) from general considerations about the observed scaling relations of early-type galaxies. The comparison of this section, however, involves uncertainties due to the fact that the tilt may depend on the sample-selection criteria. To assess if this plays an important role we perform in the next section a direct comparison of the virial predictions for the M/L derived from our own galaxy sample.

4.5 Comparison with virial predictions of M/L

An alternative way to test the validity of the virial and homology assumptions and their influence on the FP tilt is to compute the 'observed' virial $(M/L)_{\mathrm{vir}} \propto R_e \sigma_e^2 / L$ and to compare it directly to the M/L derived from the dynamical models. This has the advantage that it can be performed on our own galaxies and does not involve any choice of FP parameters or selection effects. We fitted the correlations of $(M/L)_{\mathrm{vir}}$, in the I band, with σ and with luminosity, obtaining:

$$(M/L)_{\mathrm{vir}} \propto \sigma_e^{0.82 \pm 0.07}, \tag{16}$$

$$(M/L)_{\mathrm{vir}} \propto L^{0.27 \pm 0.04}. \tag{17}$$

Equations (16) and (17) have an observed rms scatter of 19 per cent and 27 per cent, and are fully consistent with the FP determinations in equations (15) and (14), respectively. The scatter in these correlations of virial determinations is comparable to the scatter derived using the full dynamical models and, as in that case, appears dominated by the intrinsic scatter in M/L.

Finally, the most direct way of measuring the accuracy of the homology assumption is to compare $(M/L)_{\mathrm{vir}}$ with the M/L from the dynamical models. The correlation is shown in Fig. 13 and has
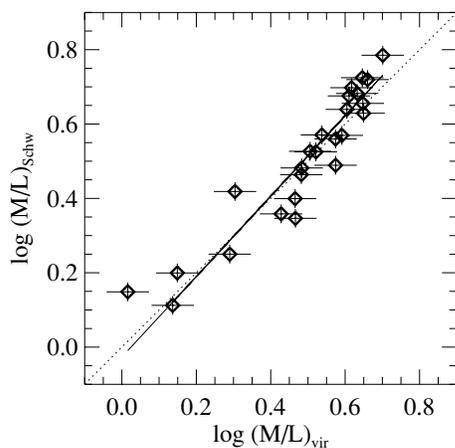
Figure 13. Comparison between the $(M/L)_{\mathrm{vir}} = \beta R_e \sigma_e^2 / (L\,G)$ derived from the virial assumption and the M/L obtained from the Schwarzschild models. The values of $(M/L)_{\mathrm{vir}}$ were scaled to match the dynamical M/L, and the best-fitting factor is $\beta = 5.0 \pm 0.1$. The solid line is a fit between the two quantities, while the dotted line represents a one-to-one correlation.

the form

$$(M/L) \propto (M/L)_{\mathrm{vir}}^{1.08 \pm 0.07}. \tag{18}$$

The observed slope is consistent with the determination based on the FP (Section 4.4), implying that both the structural and the orbital non-homology contribution cannot represent more than ~15 per cent of the FP tilt (neglecting possible selection effects in our sample, which are very difficult to estimate). Contrary to all correlations shown before, the scatter in this correlation is not influenced by the errors in the distance, as both M/L estimates use the same distance. Adopting an intrinsic accuracy of 6 per cent in the M/L determinations (Section 4.1), the scatter in $(M/L)_{\mathrm{vir}}$ required to make $\chi^2/\nu = 1$ is 14 per cent. The correlation between the virial and the Jeans estimates gives $(M/L)_{\mathrm{Jeans}} \propto (M/L)_{\mathrm{vir}}^{0.94 \pm 0.06}$ with very similar scatter to the correlation (18).

Comparing the virial and Schwarzschild M/L estimates we can provide a direct 'calibration' of the virial mass, and M/L estimator (which are often used only in a relative sense):

$$(M/L)_{\mathrm{vir}} = \frac{\beta\,R_e \sigma_e^2}{(L\,G)}. \tag{19}$$

The best-fitting scaling factor is $\beta = 5.0 \pm 0.1$. We can compare this value with the predictions from simple dynamical models, as done by a number of previous authors (e.g. Michard 1980). For this we computed the theoretical predictions for β from spherical isotropic models described by the Sérsic profile $R^{1/n}$, for different values of n. The computation was performed using high-accuracy MGE fits to the Sérsic profiles, obtained with the routines of Cappellari (2002). From the fitted MGE models, which reproduce the profiles to better than 0.05 per cent, the projected σ values can be computed with a single one-dimensional numerical integration. The projected luminosity-weighted σ was then integrated within a circular aperture of radius R_e to compute σ_e which is needed to determine the scaling factor β. In the range $n = 2$–10 the predicted β parameter is approximated to better than 3 per cent by the expression

$$\beta(n) = 8.87 - 0.831n + 0.0241n^2. \tag{20}$$

(cf. Bertin, Ciotti & Del Principe 2002). The precise value predicted for a $R^{1/4}$ profile is $\beta = 5.953$ [the value becomes $\beta = 5.872$ with a BH of 0.14 per cent of the galaxy mass as in Häring & Rix (2004)], while the observed value of $\beta \approx 5.0$ would correspond to a Sérsic index $n \approx 5.5$. However, the predictions of equation (20) only apply in an idealized situation and do not take into account the details in which $(M/L)_{\mathrm{vir}}$ is measured from real data and the fact that galaxies are not simple one-component isotropic spherical systems. From our extended photometry (Section 2.2) we measured the n values for the 25 galaxies of our sample by fitting the observed radial surface-brightness profiles. The derived Sérsic indices span the whole range $n = 2$–10 and will be presented in a future paper. From the observed variation in the profiles β should be expected to vary by a factor of ~2.5 according to the idealized spherical model. In practice, we find no significant correlation (linear correlation coefficient $r \approx -0.13$) between the measured β [the value required to make $(M/L)_{\mathrm{Schw}} = \beta R_e\,\sigma_e^2/(L\,G)$] and the one predicted by equation (20). This shows that the idealized model is not a useful representation of reality and cannot be used to try to improve the $(M/L)_{\mathrm{vir}}$ estimates. An investigation of the interesting question of why the β parameter appears so constant in real galaxies and with realistic observing conditions goes beyond the scope of the present paper.

The results of this section show that the simple virial estimate of M/L, and correspondingly of galaxy mass, is virtually unbiased, in

the sense that it produces estimates that follow a nearly one-to-one correlation with the M/L computed from much more 'expensive' dynamical models. This result has implications for high-redshift studies, as it shows, for example, that one can confidently use the virial estimator to determine masses at high redshift, where it is generally unfeasible to construct full dynamical models. It is important to emphasize, however, that this result strictly applies to virial measurements derived as we do in this paper, namely using 'classic' determination of R_e and L via $R^{1/4}$ growth curves, and with σ_e values measured in a large aperture.

4.6 Comparison with previous results

To understand whether the tight (M/L)–σ_e correlation is really due to the improved quality of the kinematical data and photometric data, we determined the observed scatter in the Johnson R-band M/L determinations by van der Marel (1991), who used a similar Jeans modelling method, on a different sample of bright elliptical galaxies (five in common with our sample). From his sample of 37 galaxies we extracted the 26 for which SBF distances by Tonry et al. (2001) exist and we performed a fit as done in Fig. 8. We used in the correlations his mean velocity dispersion $\bar{\sigma}$ and his 'improved' $(M/L)_R^{imp}$ [his column (14) from table 1 and column (18) of table 2, respectively], which we rescaled to the SBF distances, and converted to the I band assuming an R-band absolute magnitude of the Sun of $M_{R,\odot} = 4.42$ mag and a typical colour for ellipticals of $R - I \approx 0.6$, which implies $(M/L)_R/(M/L)_I \approx 1.27$. As in Section 4.2 we assumed a 5 per cent error in σ, and assigned to the M/L the errors in the SBF distance, quadratically co-added to a constant error as to make $\chi^2/\nu = 1$. The best-fitting relation is shown in Fig. 14 and has the form:

$$(M/L) = (3.54 \pm 0.17)\left(\frac{\sigma_e}{200\,\mathrm{km\,s^{-1}}}\right)^{0.79\pm0.17}, \qquad (21)$$

which is in good agreement with our equation (7), but has much larger uncertainties and an increased observed scatter of 28 per cent. This increased scatter must be attributed mainly to the differences in the quality of the data used by van der Marel (1991) and in the present paper. For the five galaxies (NGC 3379, NGC 3608,
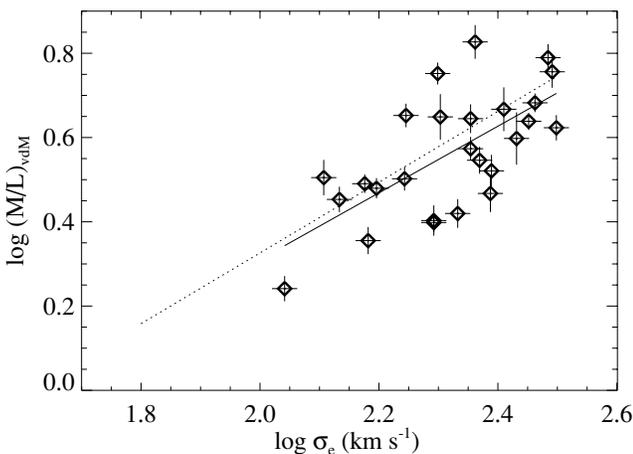
Figure 14. Same as in Fig. 8 for the M/L measurements obtained by van der Marel (1991) on a different galaxy sample. His R-band M/L values have been rescaled to the same SBF distances and zero-point we use here and converted to the I band assuming $(M/L)_R/(M/L)_I \approx 1.27$. The solid line is the best-fitting relation to the data, while the dotted line shows for comparison relation (7).

NGC 4374, NGC 4486 and NGC 5846) in common with this paper we measured relative differences $\epsilon = 1 - (M/L)_{vdM}/(M/L)_{Cap}$ of 26, 14, -11, -1 and -27 per cent, respectively.

4.7 Comparison with stellar population $(M/L)_{pop}$

We have established that the dynamical M/L can be accurately determined from our data and models, and that a tight correlation exists with σ_e, which also explains the appearance of the FP. The next obvious question is whether the observed M/L variations are mainly due to a change in the stellar population or to differences in the dark matter fraction in galaxies. A number of authors have addressed this question usually using simple dynamical models combined with stellar population models. Sometimes these investigations have produced outcomes that are not entirely consistent between each other (e.g. Kauffmann et al. 2003; Drory, Bender & Hopp 2004; Padmanabhan et al. 2004). Here we use accurate dynamical M/L and $(M/L)_{pop}$ estimates from single stellar population (SSP) models, similarly to Gerhard et al. (2001).

Using the $(M/L)_{pop}$ predictions for the SSP models[5] by Vazdekis et al. (1996, hereafter VZ96), and adopting as initial reference the Salpeter (1955) stellar initial mass function (IMF), we derived $(M/L)_{pop}$ from the SAURON Mgb, Fe5015 and Hβ line-strength indices[6] (Kuntschner et al. 2006, hereafter Paper VI). To minimize the uncertainties in the absolute calibration of the line-strength indices to model predictions, we determined the index predictions for different SSP ages and metallicities by measuring them directly on the flux-calibrated model spectral energy distributions produced by VZ99 (see discussion in Kuntschner et al. 2002). We hereby circumvent the use of the so-called Lick fitting functions which can only be used in conjunction with uncertain offsets accounting for differences in the flux calibration between models and observations. The model spectra of VZ99 were broadened to the Lick resolution using the same procedure we adopted for the SAURON spectra. In order to minimize the influence of non-solar abundance ratios we derived the $(M/L)_{pop}$ estimates from a [MgFe50] versus Hβ diagram (Fig. 15). The index [MgFe50] = $(0.45 \times \mathrm{Mg}b + \mathrm{Fe5015})/2$ is defined such that it is largely insensitive to abundance ratio variations, while Hβ is only weakly dependent on it (Trager et al. 2000; Thomas, Maraston & Korn 2004). For each galaxy, the line-strength measurements were extracted from the same high-S/N SAURON spectrum from which the σ_e were derived, that is, by luminosity weighting all the spectra within R_e (Section 2.3).

To test the robustness of the $(M/L)_{pop}$ predictions we repeated the analysis of Fig. 15 using the models of Bruzual & Charlot (2003, hereafter BC03), and those by Thomas, Maraston & Bender (2003, hereafter TMB03) and Maraston (2005), adopting the Salpeter IMF. The absolute values of the $(M/L)_{pop}$ agree to within 20 per cent between the different models over the line-strength index range relevant for our galaxies. However, the detailed agreement is better between the TMB03 and VZ96 models, while the predictions of BC03 tend to be noisier. In this paper, we choose to use the VZ96 and VZ99 models because for them predictions of the spectral
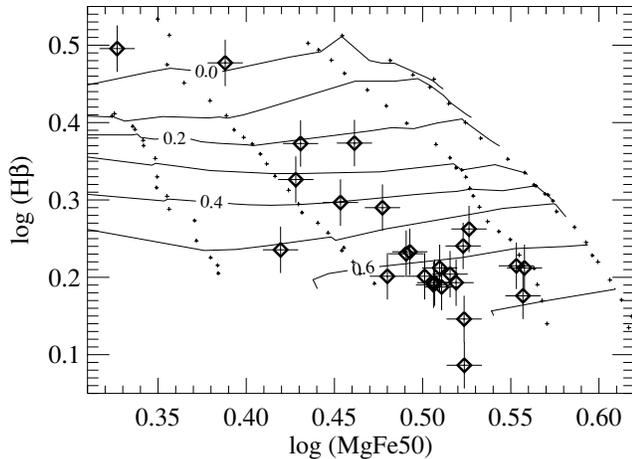
Figure 15. Observed values of the line strength index log [MgFe50] versus log (Hβ) for our galaxy sample. Overplotted are the contours showing the corresponding predictions of log(M/L)$_{pop}$ for the SSP models by VZ96 and VZ99, using the Salpeter IMF. The small crosses indicate the location where the model predictions are available, and from which the contours were linearly interpolated. Note the concentration of galaxies near the contour level log(M/L)$_{pop}$ = 0.6. The contours appear nearly horizontal in this plot, and the same is true using the Kroupa (2001) IMF. The two galaxies with the Hβ value lower than any model prediction (M87 and NGC 5846) may be contaminated by residual gas emission. Their (M/L)$_{pop}$ was estimated after increasing Hβ to the level of the model predictions.

energy distribution at moderate resolution are also available which is helpful to minimize calibration issues.

We find that for single-burst stellar populations, the contour levels of constant (M/L)$_{pop}$ in Fig. 15 tend to be nearly horizontal, in the sense that (M/L)$_{pop}$ is essentially a function of Hβ alone. This implies that, under the model assumptions, if the variations in the dynamical M/L are driven by the variation in the stellar population, a good correlation should exist between M/L and Hβ. This is tested in Fig. 16, where we plot the measured M/L and Hβ measurements and compare them to the (M/L)$_{pop}$ versus Hβ predictions, for a set of models with a large spread in age (2–17 Gyr) and metallicity ([M/H] = [−0.68, −0.38, 0.00, 0.20]). As expected from Fig. 15 the envelope of the different model curves traces a tight relation, nearly linear in logarithmic coordinates (this is less true if one also considers models with more extreme [M/H] values). The model relation follows the same trend as the data, suggesting that the variation of the stellar population is indeed an important factor in determining the observed variations of the M/L. The span of M/L from 1 to 6 mainly reflects differences in the luminosity-weighted age of the stellar population. The observed age trend is consistent with evidences of downsizing (Cowie et al. 1996) from high-redshift studies (e.g. di Serego Alighieri et al. 2005; Treu et al. 2005; van der Wel et al. 2005).

The accuracy of our M/L determinations allows us to go beyond the general agreement, to detect significant deviations, and to exclude a simple one-to-one relation between the total M/L given by the dynamical models and the (M/L)$_{pop}$ predicted by the stellar population models. In particular, for some galaxies, the measured total M/L is lower than any of the model predictions with the Salpeter IMF. For this reason, with the above caveats about the absolute scaling of the (M/L)$_{pop}$ values, and if we assume the IMF to be the same for all galaxies, we have to reject the Salpeter IMF (and any IMF with larger slope) as it gives unphysical results. Kroupa (2001)
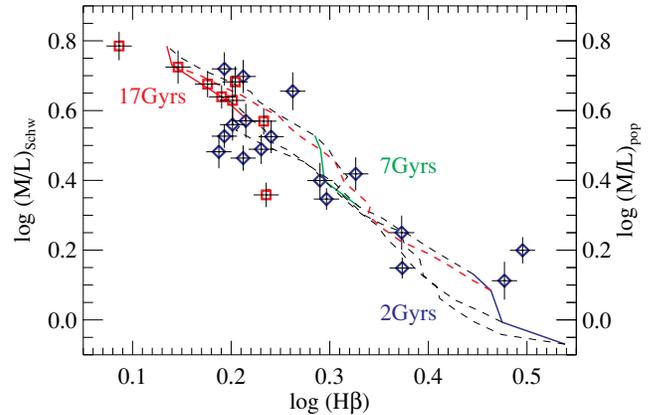
Figure 16. Observed values of the dynamical M/L versus the observed line-strength index log (Hβ). There is a clear inverse correlation between the two quantities; however, the scatter is significant, and cannot be explained by measurement errors alone. The red squares and the blue diamonds indicate slow- and fast-rotating galaxies, respectively, as defined in Table 1. The coloured lines show the predictions of log (M/L)$_{pop}$ versus log(Hβ) from the SSP models of VZ96 and VZ99, using a Salpeter IMF. The blue, green and red solid lines correspond to a model age of 2, 7 and 17 Gyr, respectively. The dashed lines indicate a metallicity [M/H] = [−0.68, −0.38, 0.00, 0.20], the red dashed line being solar metallicity [M/H] = 0. The difference in the labelling of the left-hand and right-hand axes is meant to emphasize the fact that along the vertical axis we are comparing two different quantities: the dynamical or total M/L, and the (M/L)$_{pop}$ of the stellar population alone. All the population model lines essentially overlap and define a tight relation between the two quantities, which is generally consistent with the measured trend. However, the fact that some of the measured total M/L lie below all of the population model predictions shows that the adopted IMF is unphysical. Adopting a Kroupa IMF the (M/L)$_{pop}$ model predictions decrease by ∼30 per cent [Δlog(M/L) ∼ 0.16] and all the observed M/L lie above or on top of the stellar population models. This indicates that a Kroupa IMF is consistent with the observations for all the galaxies in our sample.

has measured the IMF and constrained the shape below 1 M$_\odot$ with the result that there are fewer low-mass stars than indicated by the Salpeter law. The effect of using the Kroupa IMF is just to decrease all the (M/L)$_{pop}$ model predictions by ∼30 per cent [Δlog(M/L) ∼ 0.16]. With this IMF, none of the dynamical M/L values lie below the relation defined by the model predictions, within the measurement errors. Although we cannot independently confirm the correctness of this IMF, we adopt it for the purposes of the following discussion.

A more direct, but more model-dependent, way of looking at the relation between the stellar population and the M/L variations, is to compare M/L with (M/L)$_{pop}$ predicted using the Kroupa IMF (Fig. 17). The similarity of this figure with Fig. 16, which was obtained from the data alone, shows that the structure seen in the plot is robust, and does not come from subtle details in the SSP predictions. Again the main result is a general correlation between the total M/L and the stellar population (M/L)$_{pop}$, consistent with Gerhard et al. (2001, see their fig. 14), albeit with a smaller scatter. The relatively small scatter in the correlation indicates that the IMF of the stellar population varies little among different galaxies, consistent with the results obtained for spiral galaxies by Bell & de Jong (2001). All galaxies have (M/L)$_{pop}$ ≲ (M/L) within the errors, but the total and stellar M/L clearly do not follow a one-to-one relation (green thick line). Unless this difference between M/L and (M/L)$_{pop}$ is related to IMF variations between galaxies, it can only be caused by a change
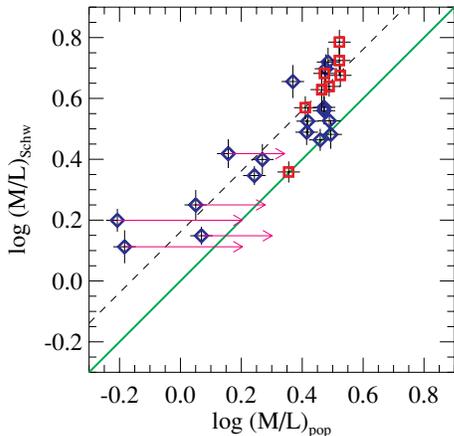
Figure 17. Dynamical (i.e. total) M/L from the Schwarzschild modelling as a function of $(M/L)_{pop}$ using the SSP models of VZ96 and VZ99, with a Kroupa (2001) IMF. The red squares and the blue diamonds indicate the slow- and fast-rotating galaxies, respectively, as defined in Table 1. The thick green line indicates the one-to-one relation. All galaxies have $(M/L)_{pop} \lesssim (M/L)$ within the errors, but the total and stellar M/L clearly do not follow a one-to-one relation. Dark matter is needed to explain the differences in M/L (if the IMF is not varying). The magenta arrows show the variation in the estimated $(M/L)_{pop}$ for the youngest galaxies (luminosity-weighted age $\lesssim 7$ Gyr), if a two-population model is assumed (see text for details). The $(M/L)_{pop}$ of the young galaxies would move closer to the one-to-one relation. Adopting the Salpeter IMF all the values of $(M/L)_{pop}$ would increase by $\Delta \log(M/L)$ ~ 0.16. This can be visualized by shifting the one-to-one relation to the position of the dashed line. In this case a number of galaxies would have $(M/L)_{pop} > (M/L)$ and this implies that the Salpeter IMF is unphysical (consistent with Fig. 16).

of dark matter fraction within[7] one R_e. The inferred median dark matter fraction is 29 per cent of the total mass, broadly consistent previous findings from dynamics (e.g. Gerhard et al. 2001; Thomas et al. 2005) and gravitational lensing (e.g. Treu & Koopmans 2004; Rusin & Kochanek 2005), implying that early-type galaxies tend to have 'minimal haloes' as spiral galaxies (Bell & de Jong 2001). The large number of galaxies in our sample with a similar value of $\log(M/L)_{pop} \sim 0.5$, and the clear evidence for a variation in the dark matter fraction in those galaxies is consistent with the result of Padmanabhan et al. (2004). However, our results are not consistent with a constancy of the $(M/L)_{pop}$ for all galaxies, and a simple dark matter variation, as we clearly detect a small number of young galaxies with low $(M/L)_{pop}$ and a correspondingly low dynamical M/L. Adopting the Salpeter IMF all the values of $(M/L)_{pop}$ would increase by $\Delta \log(M/L) \sim 0.16$. This can be visualized by moving the one-to-one relation to the position of the dashed line. In this case a number of galaxies would have $(M/L)_{pop} > (M/L)$, implying that the Salpeter IMF is unphysical (as we inferred from Fig. 16).

This analysis has been carried out in the context of SSP models. We now consider a few caveats arising from this methodology. Low-level secondary star formation can alter the values of the $(M/L)_{pop}$ derived: essentially, we underestimate $(M/L)_{pop}$ for these galaxies. This effect is expected to influence mainly the youngest galaxies, with the lowest $(M/L)_{pop}$. To estimate the importance of this effect we experimented with combinations of two SSP models, consider-

---

[7] This statement is not entirely rigorous, in fact, as shown in Section 3.3, the presence of a dark matter halo can increase the M/L measured within R_e in a way that is not simply related to the amount of dark matter within that radius.

ing a young component on top of an older solar-metallicity one. In Fig. 17, we indicate with an arrow the variation in the estimated $(M/L)_{pop}$, for the five youngest galaxies (luminosity-weighted age less than 7 Gyr), *assuming* the stellar population is composed by 90 per cent (in mass) by an old 12-Gyr population with solar metallicity and by 10 per cent by a younger population, whose age and metallicity are allowed to vary to reproduce the observed line strengths. We find that the artificial underestimation of the lowest $(M/L)_{pop}$ values can easily explain why these galaxies appear to have a high fraction of dark matter, contrary to the general trend. The adopted models use element abundances in the solar ratios, yet we know that many of our sample galaxies have enhanced ratios of Mg/Fe. Unfortunately, there are no models available which predict $(M/L)_{pop}$ as a function of abundance ratios. A possible influence on our results remains to be explored.

Given our assumptions about the IMF, we conclude the following. (i) There is a reasonable correlation between the dynamical and stellar population estimates of M/L in our sample. (ii) At low stellar M/L the overall relation is driven by age. (iii) For old galaxies there is a trend in dark matter fraction within one R_e, from zero [(M/L) $\simeq 3$] to about 30 per cent dark matter contribution for galaxies with the highest M/L in our sample [$(M/L) \simeq 6$].

5 DISCUSSION

5.1 A second parameter in the M/L variations

In this section, we investigate whether the variations in the M/L of the galaxies, apart from a main dependence on the galaxy σ_e (and closely related quantities like mass and luminosity), are also dependent on other global observables, in particular on the galaxy kinematics, morphology and environment.

As mentioned in Section 1, a number of studies over the past twenty years have suggested that early-type galaxies display a dichotomy between generally massive, slowly rotating, metal-rich galaxies and rotationally supported, less-massive, metal-poor galaxies, which suggests a difference in their formation scenarios (e.g. Davies et al. 1983; Faber et al. 1997). These differences in galaxy structure led Kormendy & Bender (1996) to propose a physically motivated revision to the classic and still broadly used (e.g. RC3) visual classification scheme by Hubble (1936), based on photometry of E and S0 galaxies, to take the findings from the kinematics into account. The fainter and faster rotating galaxies also tend to show steeper luminosity profiles than the brighter ones (Jaffe et al. 1994; Faber et al. 1997) and there is indication that they may all contain discs (Lauer et al. 2005). The SAURON kinematical maps presented in Paper III also show two general velocity field morphologies: galaxies with a clear sense of rotation, with only small kinematic twists; and galaxies with little or no rotation, or with strong kinematic misalignments. The relation between all these different galaxy properties is still not fully understood, and it will be addressed in a future paper, for the full SAURON representative sample.

Here we limit ourselves to studying the effect on the M/L of a single, hopefully representative, parameter: the galaxy kinematics. A classic and simple way to quantify the differences in galaxy kinematics is by using the anisotropy diagram (Binney 1978), which relates the observed flattening ε of a galaxy to the ratio between the ordered and random rotation of the stars (V/σ). The formalism was recently updated by Binney (2005b) for use with integral-field kinematics. The (V/σ, ε) diagram has often been used to provide a separation between fast- and slow-rotating early-type galaxies (e.g. Geha,
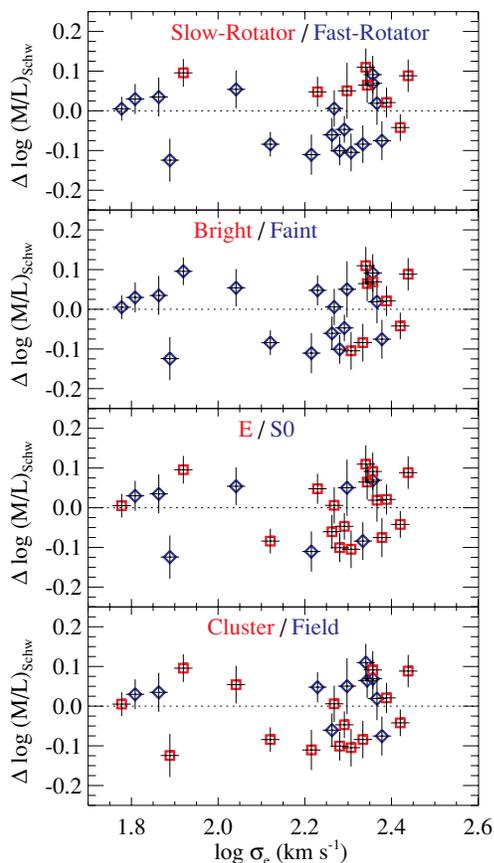
Figure 18. Residuals in the (M/L)–σ correlation of Fig. 8. The values shown are the same in the four panels, but the meaning of the red and blue symbols is different in each panel. First panel: the different galaxies are coloured according to their kinematics, using the classification in Table 1. Namely, the blue diamonds are fast-rotator galaxies, while the red squares are the slow-rotator galaxies. Second panel: the blue diamonds and red squares are the galaxies, respectively, fainter and brighter than $M_K = -24$. Third panel: here blue diamonds are S0 galaxies and red squares are E galaxies, as defined in RC3. Fourth panel: here blue diamonds are field galaxies, while red squares are cluster galaxies (as defined in Paper II). The K–S probability that the observed distribution of the residuals, for each pair of classes of objects, drawn from the same distribution is 2, 32, 74 and 10 per cent from the top to the bottom panel, respectively. The only significant difference in M/L is thus observed between the fast-rotators and the slow-rotators, while we do not detect any significant difference as a function of luminosity or morphological classification. There is some very marginal evidence for a difference in M/L as a function of environment.

Guhathakurta & van der Marel 2003). A limitation of the diagram to characterize the kinematics of a galaxy is that it contains no spatial information, so that it cannot distinguish between a fast-rotating nuclear component and a global galaxy rotation. To overcome this limitation we introduced a new *quantitative* classification scheme for early-type galaxies which is based on an approximate measure of the specific angular momentum of galaxies from integral-field stellar kinematics. In this work, we adopt that classification to define the galaxies in our sample with significant angular momentum per unit mass, which we call the 'fast-rotators' and the ones with negligible amount of specific angular momentum, which we define 'slow-rotators' (Table 1). The distinction between the two classes of galaxies can be easily seen on the kinematic maps of Paper III. More details on the classification will be given in Emsellem et al. (in preparation).

In the first (top) panel of Fig. 18 we show the distribution of the residuals in the (M/L)–σ correlation for the fast-rotators and slow-rotators, as defined above. There appears to be a tendency for the slow-rotators to have a higher M/L than the fast-rotators, at given σ_e. This difference in the distribution of the residuals between the two classes of objects can be quantified using the Kolmogorov–Smirnov (K–S) test (e.g. Press et al. 1992, section 14.3). We find that the two distributions are significantly different, the probability that they are drawn from the same distribution being 2 per cent. The same probability is found using a completely different estimator, the median statistics (Gott et al. 2001), counting the number of galaxies above and below the best-fitting relation.

A similar difference between the M/L of the slow-rotators and fast-rotators is seen with respect to the $(M/L)_{pop}$ in Fig. 17 (or Fig. 16), in the sense that the slow-rotating galaxies tend to have the largest M/L at any given $(M/L)_{pop}$ (or Hβ). If one excludes from the comparison the five youngest galaxies, and only considers the older galaxies for which the $(M/L)_{pop}$ is likely to be reliable, one finds that 7/8 of the slow-rotating galaxies lie on top or above the dashed line (which roughly corresponds to a ~30 per cent contribution of dark matter within R_e), while only 3/12 of the fast-rotating galaxies lie above the same line. In this case the probability that this difference in M/L is due to a random fluctuation is less than 1 per cent. The only slow-rotator without evidence for dark matter is NGC 4458, which appears peculiar also for being the only low-luminosity and low-σ_e slow-rotator.

In the second panel of Fig. 18 we show the dependence of the residuals of the (M/L)–σ relation on the galaxy luminosity. We separated the sample into the galaxies brighter and fainter than the K-band luminosity $M_K = -24$. This ad hoc luminosity value was chosen to have the same number of objects in the two classes as in the comparison of the top panel between fast- and slow-rotating galaxies. We do not detect any significant difference in the distribution of the residuals of the bright and faint galaxies. The K–S probability that the residuals come from the same distribution is in this case 32 per cent.

This finding that the slow-rotating galaxies, which are more common among the most massive ones (Fig. 18), have a higher M/L than the faster-rotating and, generally, less-massive ones, is reminiscent of recent findings, derived using completely different techniques, either from the dynamics of the planetary nebulae (Romanowsky et al. 2003; Napolitano et al. 2005) or from the analysis of gravitationally lensed quasars (Ferreras et al. 2005), indicating smaller fractions of dark matter among faint ellipticals, compared to more-massive ones. However, if our result is correct, it would indicate that the dark matter fraction is more closely linked to the galaxy dynamics than to the mass alone.

In the third panel of Fig. 18 we compare the distribution of the residuals in the (M/L)–σ relation for the morphologically classified E and S0 (from RC3). Consistent with previous studies (e.g. Jørgensen et al. 1996) we find no difference in the M/L distribution for the two samples. The K–S probability that the two M/L distributions are the same is in fact 74 per cent. The lack of any dependence on galaxy morphology may just reflect the limitations of the classic E/S0 visual classification, with respect to more physically motivated ones, which also consider the galaxy kinematics (e.g. Kormendy & Bender 1996).

Finally, in the fourth (bottom) panel of Fig. 18 we test whether the M/L shows a different distribution for the subsample of galaxies in clusters and in the field (defined as in Paper II). Hierarchical galaxy formation scenarios (Diaferio et al. 2001) predict that the galaxies in the field should have a significantly *lower* M/L than the galaxies

in clusters, nearly independently of redshift. From our sample we find some very marginal difference between the two distributions of residuals, the K–S probability that the two distributions are the same being 10 per cent. This small difference goes in the opposite direction than the model predictions, in the sense that the field galaxies have a marginally higher M/L than the cluster galaxies. This is consistent with recent findings from high-redshift studies, which show a similar evolution for the M/L of cluster and field galaxies (e.g. van de Ven, van Dokkum & Franx 2003; van der Wel et al. 2005). Together with the existence of the correlations we discuss in this paper, this result shows that the physical properties of the individual galaxies play a more important role in their formation and evolution than the environment.

5.2 Origin of the (M/L)–σ correlation

The (M/L)–σ_e correlation, which we studied in detail in this paper, is part of the remarkable series of tight relations of the σ_e in early-type galaxies and spiral bulges with (i) luminosity, (ii) colours, (iii) metallicity and more recently also (iv) BH mass and (v) mass of the dark halo (Ferrarese 2002). Together with these regularities, early-type galaxies are characterized by dichotomies, between the most massive giant ellipticals on one side, which are red, metal-rich, slowly rotating, and have shallow photometric profiles, and the fainter objects on the other side, which tend to be bluer, metal-poor, are dominated by rotation, have cuspy profiles and may contain discs (Davies et al. 1983; Jaffe et al. 1994; Kormendy & Bender 1996; Faber et al. 1997; Lauer et al. 2005). One way to explain the observed trends is with the standard hierarchical scenario, where galaxies are assembled from smaller building blocks. In this picture, the importance of gas during the merger process declines with increasing galaxy mass, due to the transformation of gas into stars, while galaxies are assembled. The role of the gas dissipation in the last merger could explain the observed differences in the characteristics of early-type galaxies (Bender, Burstein & Faber 1992). However, it was realized some time ago that an apparently more successful way of explaining both the regular relations and the dichotomies is to assume some form of feedback process (Dekel & Silk 1986), which must be able to stop the star formation and the chemical evolution by heating and expelling the gas from the galaxy potential well (which is related to the observed σ).

Until recently the most natural candidate feedback generator was the explosion of supernovae. But the last few years of BH studies have started to revolutionize this picture. Just five years ago the M_{BH}–σ relation first suggested a close connection between the formation of the BH and of the galaxy stellar component. Now a number of lines of evidence seem to converge towards a scenario in which the BH is the main actor in the feedback process which shapes galaxy evolution (e.g. Silk & Rees 1998; Granato et al. 2004; Binney 2005a; Loeb 2005; Ostriker & Ciotti 2005; Springel, Di Matteo & Hernquist 2005). In this picture, the gas accumulates in the dark matter potential well, feeding the BH, forming stars and enriching the medium with metals, until the BH grows to the point where its powerful jets heat and expel the gas from the galaxy. This scenario naturally explains a close connection of σ with the BH mass (Di Matteo, Springel & Hernquist 2005), as well as with the asymptotic circular velocity (related to the dark halo mass) and the M/L (related to both the halo mass and the metal enrichment).

The most obscure part of this picture is the link between the dark and the visible matter, both in the centres and the outskirts of early-type galaxies. It is remarkable that, thirty years after the first evidence of dark matter in spiral galaxies, a clear evidence of dark matter in early-type galaxies is still missing. Although a number of isolated studies from stellar dynamical models, X-ray and H I gas kinematics, or gravitational lensing indicate, not surprisingly, that early-type galaxies are also embedded in massive dark haloes, other results have challenged this picture, suggesting that some galaxies may not contain dark matter after all. In this context our work helps to constrain the elusive dark matter contribution in the central regions of galaxies. The accurate M/L determinations in galaxy centres, compared with M/L derived by kinematical tracers at large radii, are also needed to measure dark matter profiles.

Progress on the investigation of the (M/L)–σ relation can be made using: (i) larger galaxy samples, to reliably determine the intrinsic scatter and the significance of the apparent connection between the dynamics and the dark matter content in galaxies; (ii) more accurate distances [e.g. using the SBF method from the ACS Virgo Cluster Survey (Côté et al. 2004), which includes some galaxies in our sample]; and (iii) integral-field observations of samples of galaxies in clusters at intermediate distance, where the kinematics can still be resolved, but galaxies can be assumed to lie at the same distance.

5.3 Caveats

The galaxy sample we use in this paper was extracted from the SAURON representative sample of E/S0 galaxies in Paper II, and in addition includes M32 to explore the small mass regime. As described in Section 2.1, the main selection criteria were the availability of *HST* photometry and SBF distances for the galaxies, but we also excluded some obvious bars (a similar selection affects the well-known M_{BH}–σ relation). Although we have no indication that these selection criteria should bias our results in any specific way, they make the sample not necessarily representative any more. The fact that we can recover the FP correlations suggests that our small sample does represent the E/S0 population, but it is clear that increasing the galaxy modelling sample in a statistically selected way would be beneficial for future studies.

The slow-rotating galaxies that we discussed in Section 5.1 are generally thought to be triaxial (e.g. de Zeeuw & Franx 1991). If this is the case our axisymmetric models will only provide a first-order approximation to the true orbital distribution of the galaxies, and the M/L may not be correctly recovered. A significant triaxiality, however, may be expected to increase the observed scatter in the (M/L)–σ relation, which is instead quite small, arguing against strong triaxiality of the slow-rotating galaxies in our sample. This idea is also supported by the fact that these galaxies all appear quite round in projection. In any case it is not obvious that axisymmetric models of a sample of possibly triaxial galaxies, seen at random orientations, should produce a *positive* bias in the inferred M/L. A detailed test using triaxial galaxy models (Verolme et al. 2003) goes beyond the scope of the present paper.

In our models we assumed a constant M/L throughout the galaxies and in Section 3.3 we discussed the possible implications of this assumption. It is possible for the dark matter profile to vary systematically as a function of galaxy mass. As a result our constant M/L approximation would not be equally accurate for the galaxies in the different mass ranges. This effect could also produce a bias on the measured M/L, which is however difficult to quantify, given the limited information on the dark matter profiles.

The result of Section 3.3 shows, however, that it is not easy to 'hide' dark matter in the centre of galaxies. For this reason the tight (M/L)–σ correlation implies that (i) either dark matter is unimportant in galaxy centres or (ii) dark matter is closely related to the

luminous matter. In fact a dark matter halo that dominates the central regions more than the one considered [e.g. the steeper profiles found in the numerical simulations of Navarro et al. (1996)], would easily erase the correlation derived from the M/L of our models, unless the halo properties are closely linked to the stellar component. A similar conclusion was reached in a study of the tightness of the FP by Borriello, Salucci & Danese (2003).

6 CONCLUSIONS

We measured the M/L in the central regions, for a sample of 25 early-type galaxies with SAURON integral-field kinematics, using both two-integral Jeans models and three-integral Schwarzschild models. The galaxy sample was extracted from the SAURON survey (Paper II) and spans over a factor of 100 in mass. To this sample we added the galaxy M32 to explore the low-mass range. The models are constrained by SAURON kinematics, to about one effective (half-light) radius R_e, and HST/WFPC2 + MDM ground-based photometry in the I band. We studied the correlations of the M/L with global observables of the galaxies and found a sequence of increasing scatter when the M/L is correlated to: (i) the luminosity-weighted second moment of the velocity inside the half-light radius σ_e, (ii) the galaxy mass, (iii) the K-band luminosity, and (iv) the I-band luminosity. These correlations suggest that the M/L depends primarily on galaxy mass, but at a given mass it is a function of σ, which in turn is related to the galaxy compactness. For our galaxy sample the (M/L)–σ_e relation has an observed scatter of 18 per cent and an inferred intrinsic scatter of $\sim$13 per cent.

We compared the M/L derived from the dynamical models, which does not depend on any assumption of spatial or dynamical homology, with the classic predictions for the $(M/L)_{FP}$ derived from the FP, which fully depends on the assumptions of homology and virial equilibrium. The slope of our observed correlations of M/L with luminosity, mass and σ, can account for $\sim$90 per cent of the tilt of the FP. We also compared directly the M/L from the models with the virial predictions for our own sample, and found a relation $(M/L) \propto (M/L)_{vir}^{1.08\pm0.07}$, which confirms, with smaller uncertainties, the results from the FP comparisons. This also shows that, when the virial parameters R_e and L are determined in the 'classic' way, using growth curves and the σ_e is measured in a large aperture, the virial mass is a reliable and unbiased estimator of galaxy mass. This has implications for high-redshift studies, where the construction of general dynamical models is unfeasible. The best-fitting virial relation has the form $(M/L)_{vir} = (5.0 \pm 0.1) \times R_e\sigma_e^2/(LG)$, in broad agreement with simple theoretical predictions.

These correlations raise the question whether the observed M/L variations are primarily due to differences in the $(M/L)_{pop}$ of the stellar population or differences in the dark matter fraction. To test this we compared our dynamical M/L with simple estimates of the $(M/L)_{pop}$, derived from the observed line-strength indices of our galaxies. We find that the M/L generally correlates with the $(M/L)_{pop}$, indicating that the variation in the stellar population, mainly due to a variation in the luminosity-weighted age, is an important factor in driving the observed M/L variation. The relatively small scatter in the correlation indicates that the IMF of the stellar population varies little among different galaxies, consistent with results obtained for spiral galaxies by Bell & de Jong (2001). The small scatter also argues against the cuspy dark matter density profiles predicted by numerical simulations (Navarro et al. 1996).

The accuracy of our M/L determinations allows us to detect significant deviations from a one-to-one correlation, which must be due to either variations of the IMF among galaxies, or to variations in the dark matter fraction within R_e. In the latter case the median dark matter fraction for our sample is found to be $\sim$30 per cent of the total mass, broadly consistent with earlier findings from dynamics (e.g. Gerhard et al. 2001; Thomas et al. 2005) and gravitational lensing (e.g. Treu & Koopmans 2004; Rusin & Kochanek 2005). We find some evidence for the variation in M/L to be related to the dynamics of the galaxies. In particular the slow-rotating galaxies in our sample, which are more common among the most luminous objects, tend to have a higher M/L at given $(M/L)_{pop}$ than the fast-rotating and generally fainter galaxies. Assuming a constant IMF among galaxies, these results would suggest that the slow-rotating massive galaxies have a higher ($\sim$30 per cent) dark matter fraction than the fast-rotating galaxies. We speculate that this difference in M/L indicates a connection between the galaxy assembly history and the dark halo structure.

REFERENCES

Bacon R. et al., 2001, MNRAS, 326, 23 (Paper I)
Bekenstein J., 2004, Phys Rev. D, 70, 3509
Bell E. F., de Jong R. S., 2001, ApJ, 550, 212
Bender R., Burstein D., Faber S. M., 1992, ApJ, 399, 462
Bernardi M. et al., 2003, AJ, 125, 1866
Bertin G., Ciotti L., Del Principe M., 2002, A&A, 386, 149
Binney J., 1978, MNRAS, 183, 501
Binney J., 2004, in Ryder S. D., Pisano D. J., Walker M. A., Freeman K. C., eds, IAU Symp. 220, Dark Matter in Galaxies. Astron. Soc. Pac., San Francisco, p. 3
Binney J., 2005a, Phil. Trans. Roy. Soc., 363, 739
Binney J., 2005b, MNRAS, 363, 937

Binney J., Merrifield M. R., 1998, Galactic Astronomy. Princeton Univ. Press, Princeton, NJ

Binney J., Tremaine S. D., 1987, Galactic Dynamics. Princeton Univ. Press, Princeton, NJ

Binney J. J., Davies R. L., Illingworth G. D., 1990, ApJ, 361, 78

Borriello A., Salucci P., Danese L., 2003, MNRAS, 341, 1109

Bruzual G., Charlot S., 2003, MNRAS, 344, 1000 (BC03)

Burstein D., Davies R. L., Dressler A., Faber S. M., Stone R. P. S., Lynden-Bell D., Terlevich R. J., Wegner G., 1987, ApJS, 64, 601

Burstein D., Bender R., Faber S., Nolthenius R., 1997, AJ, 114, 1365

Caon N., Capaccioli M., D'Onofrio M., 1993, MNRAS, 265, 1013

Cappellari M., 2002, MNRAS, 333, 400

Cappellari M., Copin Y., 2003, MNRAS, 342, 345

Cappellari M., Emsellem E., 2004, PASP, 116, 138

Cappellari M., McDermid R. M., 2005, Class. Quantum Grav., 22, 347

Cappellari M., Verolme E. K., van der Marel R. P., Verdoes Kleijn G. A., Illingworth G. D., Franx M., Carollo C. M., de Zeeuw P. T., 2002, ApJ, 578, 787

Cappellari M. et al., 2004, in Ho L. C., ed., Carnegie Observatories Astrophys. Ser. Vol. 1, Coevolution of Black Holes and Galaxies. Carnegie Observatories, Pasadena (astro-ph/0302274)

Carollo C. M., de Zeeuw P. T., van der Marel R. P., Danziger I. J., Qian E. E., 1995, ApJ, 441, L25

Ciotti L., Lanzoni B., Renzini A., 1996, MNRAS, 282, 1

Colless M., Saglia R. P., Burstein D., Davies R. L., McMahan R. K., Wegner G., 2001, MNRAS, 321, 277

Côté P. et al., 2004, ApJS, 153, 223

Cowie L. L., Songaila A., Hu E. M., Cohen J. G., 1996, AJ, 112, 839

Cretton N., de Zeeuw P. T., van der Marel R. P., Rix H.-W., 1999, ApJS, 124, 383

Davies R. L., Efstathiou G. P., Fall S. M., Illingworth G. D., Schechter P. L., 1983, APJ, 266, 41

Dekel A., Silk J., 1986, ApJ, 303, 39

de Vaucouleurs G., de Vaucouleurs A., Corwin H. G., Buta R. J., Paturel G., Fouque P., 1991, Third Reference Catalogue of Bright Galaxies. Springer-Verlag, New York (RC3)

de Zeeuw P. T., Franx M., 1991, ARA&A, 29, 239

de Zeeuw P. T. et al., 2002, MNRAS, 329, 513 (Paper II)

Diaferio A., Kauffmann G., Balogh M. L., White S. D. M., Schade D., Ellingson E., 2001, MNRAS, 323, 999

Di Matteo T., Springel V., Hernquist L., 2005, Nat, 433, 604

di Serego Alighieri S. et al., 2005, A&A, 442, 125

Djorgovski S., Davis M., 1987, ApJ, 313, 59

Dolphin A. E., 2000, PASP, 112, 1397

Dressler A., Lynden-Bell D., Burstein D., Davies R. L., Faber S. M., Terlevich R., Wegner G., 1987, ApJ, 313, 42

Drory N., Bender R., Hopp U., 2004, ApJ, 616, L103

Emsellem E., Monnet G., Bacon R., 1994, A&A, 285, 723

Emsellem E. et al., 2004, MNRAS, 352, 721 (Paper III)

Faber S. M., Jackson R. E., 1976, ApJ, 204, 668

Faber S. M., Dressler A., Davies R. L., Burstein D., Lynden-Bell D., Terlevich R. J., Wegner G., 1987, in Faber S. M., ed., Nearly Normal Galaxies. Springer-Verlag, New York, p. 175

Faber S. M. et al., 1997, AJ, 114, 1771

Ferrarese L., 2002, ApJ, 578, 90

Ferrarese L., Merritt D., 2000, ApJ, 539, L9

Ferreras I., Saha P., Williams L. L. R. 2005, ApJ, 623, L5

Forbes D. A., Ponman T. J., Brown R. J. N., 1998, ApJ, 508, L43

Forbes D. A., Ponman T. J., 1999, MNRAS, 309, 623

Franx M., Illingworth G. D., de Zeeuw P. T., 1991, ApJ, 383, 112

Freedman W. L. et al., 2001, ApJ, 553, 47

Gebhardt K. et al., 2000, ApJ, 539, L13

Gebhardt K. et al., 2003, ApJ, 583, 92

Geha M., Guhathakurta P., van der Marel R. P., 2003, AJ, 126, 1794

Gerhard O. E., 1993, MNRAS, 265, 213

Gerhard O., Kronawitter A., Saglia R. P., Bender R., 2001, AJ, 121, 1936

Gott J. R. I., Vogeley M. S., Podariu S., Ratra B., 2001, ApJ, 549, 1

Graham A., Colless M., 1997, MNRAS, 287, 221

Graham A. W., Guzmán R., 2003, AJ, 125, 2936

Graham A. W., Trujillo I., Caon N., 2001, AJ, 122, 1707

Granato G. L., De Zotti G., Silva L., Bressan A., Danese L., 2004, ApJ, 600, 580

Hairer E., Norsett S. P., Wanner G., 1993, Solving Ordinary Differential Equations I. Nonstiff Problems, Springer Series in Comput. Mathematics, 2nd edn. Springer-Verlag, Berlin

Häring N., Rix H.-W., 2004, ApJ, 604, L89

Hernquist L., 1990, ApJ, 356, 359

Hoaglin D. C., Mosteller F., Tukey J. W., 1983, Understanding Robust and Exploratory Data Analysis. Wiley, New York

Hubble E. P., 1936, The Realm of the Nebulae. Yale Univ. Press

Hunter C., 1977, AJ, 82, 271

Jaffe W., Ford H. C., O'Connell R. W., van den Bosch F. C., Ferrarese L., 1994, AJ, 108, 1567

Jarrett T. H., Chester T., Cutri R., Schneider S., Skrutskie M., Huchra J. P., 2000, AJ, 119, 2498

Jørgensen I., Franx M., Kjaergaard P., 1995, MNRAS, 273, 1097

Jørgensen I., Franx M., Kjaergaard P., 1996, MNRAS, 280, 167

Kauffmann G. et al., 2003, MNRAS, 341, 33

Kormendy J., Bender R., 1996, ApJ, 464, L119

Kormendy J., Gebhardt K., 2001, AIP Conf., 586, 383

Krajnović D., Cappellari M., Emsellem E., McDermid R., de Zeeuw P. T., 2005, MNRAS, 357, 1113

Kroupa P., 2001, MNRAS, 322, 231

Kuntschner H., Smith R. J., Colless M., Davies R. L., Kaldare R., Vazdekis A., 2002, MNRAS, 337, 172

Kuntschner H. et al. 2006, MNRAS, submitted (Paper VI)

Landsman W. B., 1993, in Hanisch R. J., Brissenden R. J. V., Barnes J., eds, ASP Conf. Ser. Vol. 52, Astronomical Data Analysis Software and Systems II. Astron. Soc. Pac., San Francisco, p. 246

Lanzoni B., Ciotti L., Cappi A., Tormen G., Zamorani G., 2004, ApJ, 600, 640

Lauer T. et al., 2005, AJ, 129, 2138

Lynden-Bell D., 1962, MNRAS, 123, 447

Loeb A., 2005, in Merloni A., Nayakshin S., Sunyaev R., eds, Growing Black Holes. Springer, Berlin, p. 18

Magorrian J. et al., 1998, AJ, 115, 2285

Maraston C., 2005, MNRAS, 362, 799

Marconi A., Hunt L. K., 2003, ApJ, 589, L21

Mehlert D., Thomas D., Saglia R. P., Bender R., Wegner G., 2003, A&A, 407, 423

Mei S. et al., 2005, ApJ, 625, 121

Michard R., 1980, A&A, 91, 122

Milgrom M., 1983, ApJ, 270, 365

Monnet G., Bacon R., Emsellem E., 1992, A&A, 253, 366

Napolitano N. R. et al., 2005, MNRAS, 357, 691

Navarro J. F., Frenk C. S., White S. D. M., 1996, ApJ, 462, 563

Ostriker J. P., Ciotti L., 2005, Phil. Trans. Roy. Soc., 363, 667

Padmanabhan N. et al., 2004, New. Astron., 9, 329

Pahre M. A., Djorgovski S. G., de Carvalho R. R., 1998, AJ, 116, 1591

Press W. H., Teukolsky S. A., Vetterling W. T., Flannery B. P., 1992, Numerical Recipes in FORTRAN 77, 2nd edn. Cambridge Univ. Press, Cambridge

Prugniel P., Simien F., 1996, A&A, 309, 749

Prugniel P., Simien F., 1997, A&A, 321, 111

Richstone D. O., Tremaine S., 1988, ApJ, 327, 82

Rix H., de Zeeuw P. T., Cretton N., van der Marel R. P., Carollo C. M., 1997, ApJ, 488, 702

Romanowsky A. J., Douglas N. G., Arnaboldi M., Kuijken K., Merrifield M. R., Napolitano N. R., Capaccioli M., Freeman K. C., 2003, Sci, 301, 1696

Rusin D., Kochanek C. S., 2005, ApJ, 623, 666

Rybicki G. B., 1987, in de Zeeuw P. T., ed., IAU Symp. 127, Structure and Dynamics of Elliptical Galaxies. Reidel, Dordrecht, p. 397

Salpeter E. E., 1955, ApJ, 121, 161

Sarzi M. et al., 2006, MNRAS, in press (doi:10.1111/j.1365-2966.2005.09839.x) (Paper V, this issue) (astro/ph/0511307)

Satoh C., 1980, PASJ, 32, 41

Schlegel D. J., Finkbeiner D. P., Davis M., 1998, ApJ, 500, 525

Schwarzschild M., 1979, ApJ, 232, 236

Scodeggio M., Giovanelli R., Haynes M. P., 1997, AJ, 113, 101

Sérsic J. L., 1968, Atlas de galaxias australes. Observatorio Astronomico, Cordoba, Argentina

Silk J., Rees M., 1998, A&A, 331, L1

Springel V., Di Matteo T., Hernquist L., 2005, ApJ, 620, L79

Thomas D., Maraston C., Bender R., 2003, MNRAS, 339, 897 (TMB03)

Thomas D., Maraston C., Korn A., 2004, MNRAS, 351, L19

Thomas J., Saglia R. P., Bender R., Thomas D., Gebhardt K., Magorrian J., Richstone D., 2004, MNRAS, 353, 391

Thomas J., Saglia R. P., Bender R., Thomas D., Gebhardt K., Magorrian J., Corsini E. M., Wegner G., 2005, MNRAS, 360, 1355

Tonry J. L., Dressler A., Blakeslee J. P., Ajhar E. A., Fletcher A. B., Luppino G. A., Metzger M. R., Moore C. B., 2001, ApJ, 546, 681

Trager S. C., Faber S. M., Worthey G., González J. J., 2000, AJ, 120, 165

Tremaine S., Richstone D. O., Byun Y., Dressler A., Faber S. M., Grillmair C., Kormendy J., Lauer T. R., 1994, AJ, 107, 634

Tremaine S. et al., 2002, ApJ, 574, 740

Tremblay B., Merritt D., 1996, AJ, 111, 2243

Treu T., Koopmans L. V. E., 2004, ApJ, 611, 739

Treu T., Ellis R. S., Liao T. X., van Dokkum P. G., 2005, ApJ, 622, L5

Trujillo I., Graham A. W., Caon N., 2001, MNRAS, 326, 869

Trujillo I., Burkert A., Bell E. F., 2004, ApJ, 600, L39

Valluri M., Merritt D., Emsellem E., 2004, ApJ, 602, 66

van Albada T. S., Bertin G., Stiavelli M., 1995, MNRAS, 276, 1255

van der Marel R. P., 1991, MNRAS, 253, 710

van der Marel R. P., 1994, MNRAS, 270, 271

van der Marel R. P., Franx M., 1993, ApJ, 407, 525

van der Marel R. P., Cretton N., de Zeeuw P. T., Rix H., 1998, ApJ, 493, 613

van de Ven G., van Dokkum P. G., Franx M., 2003, MNRAS, 344, 924

van der Wel A., Franx M., van Dokkum P. G., Rix H.-W., Illingworth G. D., Rosati P., 2005, ApJ, 631, 145

Vazdekis A., 1999, ApJ, 513, 224 (VZ99)

Vazdekis A., Casuso E., Peletier R. F., Beckman J. E., 1996, ApJS, 106, 307 (VZ96)

Verolme E. K. et al., 2002, MNRAS, 335, 517

Verolme E. K., Cappellari M., van de Ven G., de Zeeuw P. T., 2003, in Contopoulos G., Voglis N., eds, Lecture Notes In Physics Vol. 626, Galaxies and Chaos. Springer, Berlin, p. 279

Zaritsky D., Gonzalez A. H., Zabludoff A. I., 2005, ApJ, in press (astro-ph/0510221)

APPENDIX A: CONSTRAINTS ON INCLINATION FROM TWO-INTEGRAL MODELS

In this appendix we present the Jeans two-integral models of five galaxies in our sample, for which the inclination can be independently determined by non-dynamical arguments. The galaxies NGC 524 and NGC 4459 possess very regular dust discs, while NGC 4150 has a more disturbed disc, which are all clearly visible on the unsharp-masked *HST*/WFPC2 images (fig. 4 of Sarzi et al. 2006, hereafter Paper V). We fitted an ellipse to the dust morphology, and, assuming the discs are intrinsically circular, and in equilibrium in the equatorial plane of an oblate spheroid, we inferred an inclination of $i = 20° \pm 5°$, $54° \pm 5°$ and $46° \pm 2°$, respectively, for NGC 524, NGC 4150 and NGC 4459. The inclination of the gas disc in NGC 2974 was carefully studied by Krajnović et al. (2005) who derived an inclination of $i = 60° \pm 3°$. Finally, in the case of NGC 4552 there is no evidence of extended patchy dust absorption, but this giant elliptical is unlikely to be intrinsically very flat (see discussion

in Section 3.2). We expect a broad range of possible inclinations, but low values should be excluded.

In Fig. A1, we compare the maps of the observed projected second moment of the velocity $\mu'_2 \equiv \sqrt{V^2 + \sigma^2}$, as derived from the SAURON stellar kinematics, with the maps of the unique second velocity moment associated to the MGE density distribution, computed by solving the Jeans equations, at every inclination. To help the visual comparison between data and models, the observed μ'_2 was bi-symmetrized by replacing the value in each bin with the average of the corresponding values in the four quadrants (computed using linear interpolation). Each plot is scaled to the best-fitting M/L using equation (2). This same kind of fit was performed for all the 25 galaxies in the sample, to determine the inclination at which the M/L of the Jeans and Schwarzschild models was measured. The Jeans models always provide a clear best-fitting value for the inclination, which can also be easily recognized by eye. Starting from an edge-on model ($i = 90°$), the effect of lowering the inclination (while keeping the M/L at the best-fitting value) can be mainly described as a decrease of the second moments along the minor axis, accompanied by a corresponding increase along the major axis. For the five galaxies considered in this appendix the best-fitting inclination derived from the Jeans models agrees with the expected values.

APPENDIX B: MULTI-GAUSSIAN EXPANSION PARAMETERS OF THE SAMPLE

In this appendix (Tables B1–B2) we present the (distance-independent) numerical values of the analytically deconvolved MGE parametrization of the surface brightness of the galaxies in our sample.[8] The constant-PA models were obtained by fitting the *HST*/WFPC2/*F814W* photometry at small radii and the ground-based MDM photometry (in the same band) at large radii. They provide an accurate description of the *I*-band surface brightness of the galaxies from $R \approx 0.01$ arcsec to about twice the maximum σ_j used in each galaxy (usually corresponding to 5–10 R_e). The nucleus of NGC 4150 is heavily obscured by dust. For this galaxy we fitted the nuclear MGE model to an *HST*/NICMOS/F160W (*H*-band) image, which was rescaled to the WFPC2/*F814W* (*I*-band) one for calibration, neglecting possible $I − H$ color gradients. In other galaxies dust and bright foreground stars were simply excluded from the MGE fit. The matching of the different images and the calibration adopted for the MGE models is described in Section 3.1. The deconvolved MGE surface brightness Σ is defined as follows:

$$\Sigma(x', y') = \sum_{j=1}^{N} I'_j \exp \left[-\frac{1}{2\sigma_j^2} \left(x'^2 + \frac{y'^2}{q_j'^2} \right) \right], \qquad (B1)$$

where the model is composed by N Gaussian components of dispersion σ_j, axial ratio q'_j and peak intensity I'_j. The coordinates (x', y') are measured on the sky plane, with the x'-axis corresponding to the galaxy major axis. The total luminosity of each Gaussian component is given by $L_j = 2\pi I'_j \sigma_j^2 q'_j$ (see Cappellari 2002, for details).

---

[8] The values for the MGE parametrization of NGC 2974 were given in Krajnović et al. (2005)
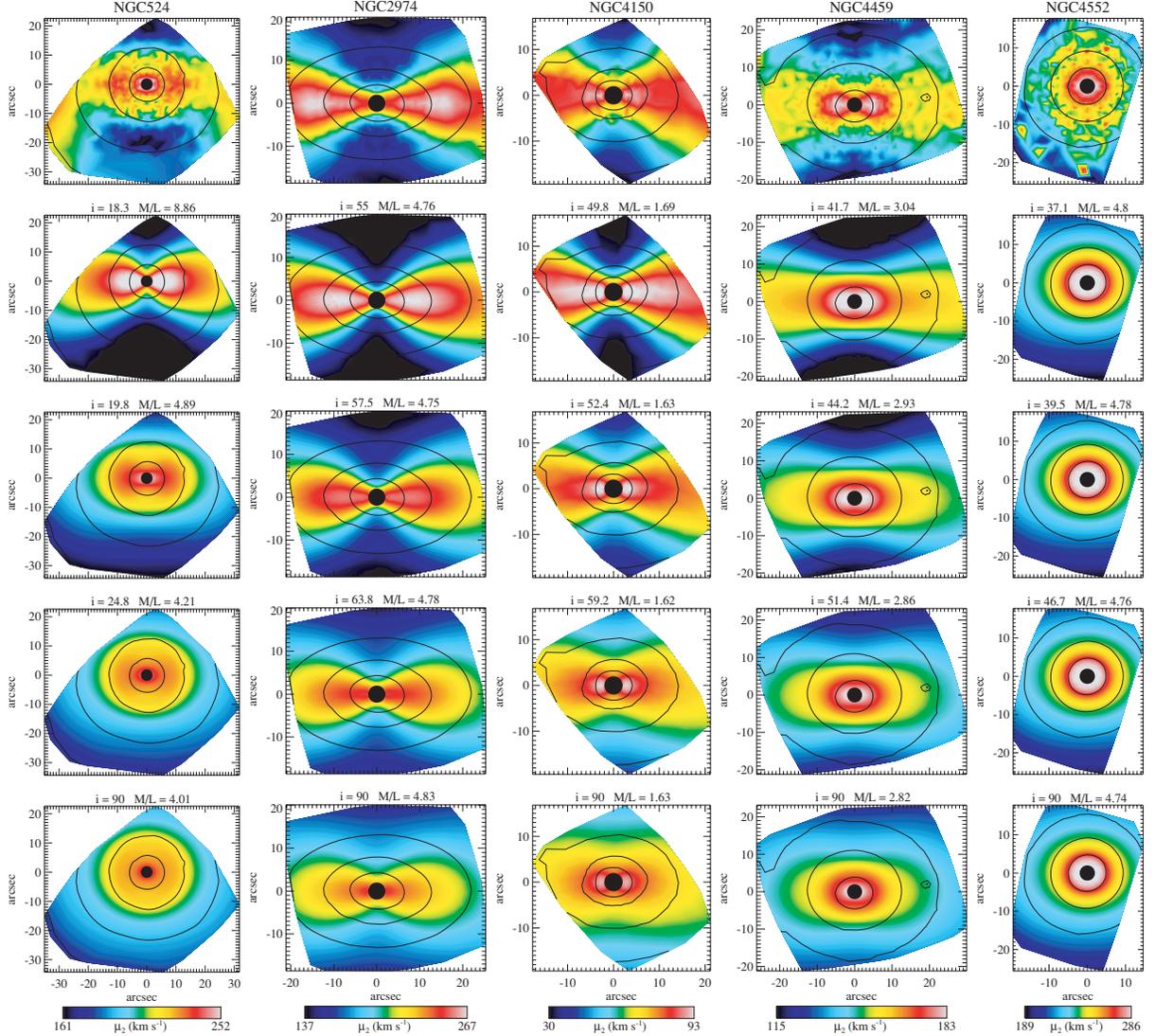
Figure A1. Top panels: bi-symmetrized and linearly interpolated map of the observed second velocity moment $\mu_2' \equiv \sqrt{V^2 + \sigma^2}$, extracted from the SAURON stellar kinematics of the galaxies NGC 524, NGC 2974, NGC 4150, NGC 4459 and NGC 4552. The actual Voronoi bins in which the kinematics was measured are shown in Paper III. The black central disc shows the region that was excluded from the following fits. Subsequent panels: two-integral Jeans modelling of the unique projected second moments associated to the MGE mass density distribution, for different inclinations. Each plot is scaled to the best-fitting M/L using equation (2). For every galaxy the lowest inclination corresponds to an intrinsic axial ratio $q = 0.1$ of the flattest Gaussian component in the MGE model. Subsequent panels are equally spaced in q. The inclination of each model, and the corresponding best-fitting M/L is written above each plot. The inclination independently inferred from the geometry of the dust or from the gas kinematics is $i \approx 20°$, $60°$, $54°$ and $46°$, for NGC 524, NGC 2974, NGC 4150 and NGC 4459, respectively. No strong constraint exists for the inclination of NGC 4552, but this giant elliptical is not expected to be flat (see Section 3.2), so it should be best fitted for $i \approx 90°$. For all the five galaxies the best-fitting inclination derived from the Jeans models agrees with the expected value, as can also be seen by eye on these maps.

Table B1. MGE parameters for the deconvolved *I*-band surface brightness.

j	$\log I'_j$ $(\mathrm{L}_{\odot,I}\,\mathrm{pc}^{-2})$	$\log \sigma_j$ (arcsec)	q'_j	$\log I'_j$ $(\mathrm{L}_{\odot,I}\,\mathrm{pc}^{-2})$	$\log \sigma_j$ (arcsec)	q'_j	$\log I'_j$ $(\mathrm{L}_{\odot,I}\,\mathrm{pc}^{-2})$	$\log \sigma_j$ (arcsec)	q'_j	$\log I'_j$ $(\mathrm{L}_{\odot,I}\,\mathrm{pc}^{-2})$	$\log \sigma_j$ (arcsec)	q'_j
	NGC 221			NGC 524			NGC 821			NGC 3156		
1	6.187	−1.762	0.790	4.336	−1.762	0.950	5.322	−1.526	0.706	6.103	−1.762	0.700
2	5.774	−1.143	0.741	3.807	−1.199	0.950	4.922	−0.954	0.703	5.236	−1.464	0.700
3	5.766	−0.839	0.786	4.431	−0.525	0.950	4.608	−0.586	0.621	4.991	−1.015	0.700
4	5.613	−0.438	0.757	3.914	−0.037	0.950	4.294	−0.283	0.625	4.027	−0.744	0.700
5	5.311	−0.104	0.720	3.638	0.327	0.950	4.059	−0.003	0.601	3.857	−0.604	0.400
6	4.774	0.232	0.724	3.530	0.629	0.950	3.860	0.260	0.643	4.275	−0.523	0.700
7	4.359	0.560	0.725	3.073	1.082	0.950	3.446	0.574	0.586	3.577	−0.036	0.579
8	4.087	0.835	0.743	2.450	1.475	0.950	3.071	0.787	0.776	3.011	0.374	0.700
9	3.682	1.160	0.751	1.832	1.708	0.950	2.560	1.002	0.300	2.698	0.776	0.491
10	3.316	1.414	0.838	1.300	2.132	0.950	2.741	1.190	0.585	2.466	1.011	0.582
11	2.744	1.703	0.835	–	–	–	2.244	1.485	0.662	2.235	1.276	0.404
12	1.618	2.249	0.720	–	–	–	1.482	1.734	0.758	1.761	1.580	0.590
13	–	–	–	–	–	–	1.235	2.068	0.800	–	–	–
	NGC 3377			NGC 3379			NGC 3414			NGC 3608		
1	6.042	−1.664	0.740	4.264	−1.314	0.900	5.924	−1.704	0.801	4.387	−1.340	0.900
2	5.444	−0.993	0.741	4.210	−0.771	0.900	4.990	−1.028	0.800	4.386	−0.892	0.892
3	4.836	−0.604	0.469	4.182	−0.197	0.926	4.663	−0.628	0.817	4.376	−0.566	0.890
4	4.837	−0.590	0.713	4.167	0.045	0.895	4.353	−0.262	0.791	4.244	−0.237	0.834
5	4.173	−0.324	0.900	3.939	0.340	0.850	3.906	0.136	0.711	3.944	0.077	0.844
6	4.618	−0.154	0.402	3.907	0.493	0.929	3.610	0.449	0.741	3.295	0.325	0.807
7	4.151	0.118	0.464	3.354	0.782	0.852	3.109	0.769	0.791	3.378	0.533	0.798
8	3.424	0.293	0.807	3.455	0.870	0.967	2.675	0.982	0.855	3.112	0.831	0.815
9	3.760	0.463	0.345	2.902	1.111	0.850	2.345	1.308	0.664	2.400	1.174	0.750
10	3.458	0.657	0.461	2.728	1.430	0.866	2.041	1.555	0.846	2.276	1.459	0.781
11	3.226	0.883	0.523	2.287	1.685	0.850	1.258	1.973	0.980	1.550	1.977	0.881
12	2.813	1.235	0.455	1.645	2.008	0.901	–	–	–	–	–	–
13	2.479	1.423	0.546	1.108	2.400	0.861	–	–	–	–	–	–
14	1.895	1.686	0.559	–	–	–	–	–	–	–	–	–
15	1.632	1.811	0.800	–	–	–	–	–	–	–	–	–
16	1.165	2.172	0.899	–	–	–	–	–	–	–	–	–
	NGC 4150			NGC 4278			NGC 4374			NGC 4458		
1	5.231	−1.421	0.990	5.147	−1.637	0.800	4.172	−1.762	0.990	4.772	−1.100	0.250
2	4.528	−0.732	0.990	4.146	−0.320	0.800	4.974	−1.762	0.990	4.970	−0.954	0.250
3	4.421	−0.404	0.990	4.030	0.002	0.900	4.398	−1.093	0.990	2.748	−0.852	0.643
4	4.000	−0.009	0.990	3.877	0.170	0.800	3.919	0.085	0.800	4.657	−0.655	0.533
5	3.676	0.326	0.701	3.784	0.423	0.842	4.080	0.412	0.800	4.233	−0.378	0.604
6	2.916	0.479	0.880	3.544	0.774	0.846	3.735	0.758	0.814	3.747	−0.106	0.666
7	2.947	0.814	0.674	3.043	1.059	0.898	3.199	1.043	0.838	3.297	0.145	0.752
8	2.275	1.229	0.650	2.471	1.440	0.900	2.847	1.331	0.874	3.026	0.416	0.834
9	2.216	1.365	0.650	1.748	1.766	0.900	2.425	1.592	0.935	2.823	0.697	0.870
10	1.023	1.787	0.660	1.189	2.182	0.857	1.953	1.894	0.990	2.362	1.020	0.873
11	–	–	–	–	–	–	1.509	2.259	0.990	2.033	1.344	0.950
12	–	–	–	–	–	–	–	–	–	0.988	1.973	0.950

Table B2. MGE parameters for the deconvolved *I*-band surface brightness.

j	$\log I'_j$ (L$_{\odot,I}$ pc^{-2})	$\log \sigma_j$ (arcsec)	q'_j	$\log I'_j$ (L$_{\odot,I}$ pc^{-2})	$\log \sigma_j$ (arcsec)	q'_j	$\log I'_j$ (L$_{\odot,I}$ pc^{-2})	$\log \sigma_j$ (arcsec)	q'_j	$\log I'_j$ (L$_{\odot,I}$ pc^{-2})	$\log \sigma_j$ (arcsec)	q'_j
	NGC 4459			NGC 4473			NGC 4486			NGC 4526		
1	5.592	−1.737	0.820	4.346	−1.762	0.550	6.541	−1.762	0.950	5.463	−1.230	0.900
2	5.463	−1.507	0.820	3.900	−1.137	0.545	4.738	−0.971	0.955	4.610	−0.441	0.900
3	4.947	−0.928	0.817	4.277	−0.623	0.555	3.513	−0.415	0.944	4.223	−0.067	0.900
4	4.560	−0.513	0.929	4.207	−0.315	0.528	3.288	0.007	0.990	4.049	0.470	0.474
5	4.504	−0.197	0.949	4.134	−0.021	0.491	3.375	0.520	0.990	3.748	0.629	0.651
6	3.731	0.115	0.933	3.755	0.212	0.750	3.468	0.834	0.990	3.379	0.969	0.678
7	3.706	0.370	0.822	3.883	0.306	0.400	3.209	1.114	0.967	3.003	1.329	0.635
8	3.223	0.396	0.990	3.654	0.534	0.686	2.862	1.389	0.949	1.198	1.683	0.900
9	3.362	0.765	0.879	3.529	0.583	0.400	2.460	1.731	0.886	2.253	1.718	0.273
10	2.968	1.021	0.830	3.372	0.833	0.537	1.671	1.906	0.990	2.169	1.938	0.262
11	2.631	1.303	0.795	3.078	0.849	0.750	1.671	2.166	0.700	1.594	2.048	0.438
12	2.109	1.638	0.750	2.922	1.153	0.541	1.153	2.515	0.700	0.558	2.264	0.900
13	1.632	1.891	0.990	2.483	1.421	0.532	–	–	–	–	–	–
14	–	–	–	2.149	1.662	0.572	–	–	–	–	–	–
15	–	–	–	1.639	1.989	0.654	–	–	–	–	–	–
	NGC 4450			NGC 4552			NGC 4621			NGC 4660		
1	5.384	−1.596	0.600	5.064	−1.762	0.990	5.797	−1.397	0.800	5.984	−1.620	0.900
2	4.724	−1.038	0.600	4.282	−0.396	0.800	5.323	−1.030	0.798	5.138	−1.071	0.900
3	4.181	−0.643	0.600	4.325	−0.339	0.990	4.956	−0.701	0.773	4.853	−0.763	0.533
4	4.067	−0.501	0.372	4.209	−0.057	0.957	4.557	−0.415	0.950	4.709	−0.541	0.671
5	3.891	−0.234	0.600	4.153	0.223	0.933	4.200	−0.159	0.321	4.336	−0.209	0.546
6	3.416	0.208	0.554	3.784	0.594	0.948	4.138	−0.062	0.893	3.997	−0.182	0.900
7	3.046	0.647	0.600	3.416	0.860	0.975	3.838	0.241	0.819	4.187	0.154	0.450
8	3.218	0.815	0.289	2.711	1.187	0.887	3.900	0.295	0.295	3.946	0.346	0.590
9	2.847	1.053	0.385	2.608	1.389	0.928	3.607	0.589	0.743	3.319	0.590	0.730
10	2.770	1.117	0.228	1.992	1.725	0.884	3.317	0.656	0.302	2.862	0.697	0.900
11	2.487	1.381	0.320	1.540	2.136	0.990	3.319	0.886	0.755	3.163	0.981	0.450
12	1.866	1.480	0.394	–	–	–	2.538	1.094	0.333	2.152	1.148	0.900
13	1.315	1.686	0.183	–	–	–	2.885	1.277	0.635	2.417	1.265	0.450
14	1.029	1.867	0.600	–	–	–	2.461	1.544	0.628	1.930	1.451	0.779
15	1.007	1.867	0.153	–	–	–	1.639	1.812	0.926	1.243	1.806	0.878
16	–	–	–	–	–	–	1.706	1.849	0.472	–	–	–
17	–	–	–	–	–	–	1.379	2.190	0.950	–	–	–
	NGC 5813			NGC 5845			NGC 5846			NGC 7457		
1	3.645	−0.457	0.980	5.559	−1.762	0.800	3.647	−1.762	0.990	6.308	−1.762	0.900
2	3.913	−0.262	0.980	5.229	−1.271	0.800	3.794	0.167	0.990	4.778	−1.059	0.900
3	3.848	−0.026	0.900	4.688	−1.049	0.462	3.125	0.449	0.990	4.056	−0.680	0.900
4	3.755	0.254	0.885	4.400	−0.567	0.800	3.334	0.725	0.990	3.702	−0.424	0.900
5	3.401	0.522	0.924	4.197	−0.184	0.768	2.772	1.063	0.969	3.653	−0.132	0.696
6	2.962	0.810	0.909	4.232	0.015	0.263	2.625	1.289	0.974	3.451	0.172	0.703
7	2.516	1.024	0.882	3.862	0.063	0.708	1.946	1.526	0.850	3.174	0.495	0.613
8	2.264	1.336	0.784	3.710	0.237	0.668	1.984	1.777	0.924	2.541	0.812	0.528
9	2.180	1.623	0.721	3.629	0.459	0.800	1.431	2.197	0.850	2.535	0.939	0.655
10	0.706	2.063	0.980	2.632	0.664	0.538	–	–	–	2.520	1.256	0.555
11	1.467	2.063	0.720	2.909	0.820	0.564	–	–	–	2.236	1.628	0.517
12	–	–	–	2.127	1.206	0.708	–	–	–	1.369	1.958	0.774

This paper has been typeset from a T$_{\rm E}$X/L$^{\!A}$T$_{\rm E}$X file prepared by the author.